https://doi.org/10.5194/egusphere-2026-2210
Preprint. Discussion started: 8 May 2026

Bias in satellite-derived cloud radiative effect over Arctic sea ice relative to aircraft measurements during ARCSIX

Sebastian Becker[1,2], Konrad Sebastian Schmidt[3,4], Hong Chen[4], Yu-Wen Chen[3,4], Kerry G. Meyer[5], Colten A. Peterson[5,6], and Manfred Wendisch[1]

[1]Leipzig Institute for Meteorology, Leipzig University, Leipzig, Germany
[2]Institute of Geophysics and Meteorology, University of Cologne, Cologne, Germany
[3]Department of Atmospheric and Oceanic Sciences, University of Colorado, Boulder, CO, USA
[4]Laboratory for Atmospheric and Space Physics, University of Colorado, Boulder, CO, USA
[5]NASA Goddard Space Flight Center, Greenbelt, MD, USA
[6]Goddard Earth Sciences Technology and Research II, University of Maryland-Baltimore County, Baltimore, MD, USA

Correspondence: Konrad Sebastian Schmidt (Sebastian.Schmidt@lasp.colorado.edu) and Sebastian Becker (sebastian.becker@uni-koeln.de)

Abstract. The surface radiation budget (SRB) strongly controls the summertime evolution of sea ice and, therefore, plays a key role for the ongoing transformations of the Arctic climate system. Clouds can have a significant impact on the SRB, which is quantified by the cloud radiative effect (CRE). Consequently, continuous, Arctic-wide monitoring of clouds and further factors governing the CRE, including surface and thermodynamic properties, is required. These persistent observations can only be provided by passive remote sensing instruments aboard polar-orbiting satellites. However, cloud detection deficiencies and the lack of accurate surface albedo data over heterogeneous sea ice limit the precision of satellite products and subsequent CRE estimates. Therefore, this study quantifies the accuracy of satellite cloud products, the surface albedo assumed therein, thermodynamic analysis data, and the resulting CRE simulations. To isolate the contributions of individual parameters to the CRE bias, satellite-derived simulation input is consecutively replaced with collocated aircraft observations that were collected over sea ice north of Greenland during the Arctic Radiation–Cloud–Aerosol–Surface Interaction Experiment (ARCSIX) between May and August 2024. It is concluded that clouds warm the surface according to simulations initialized with aircraft measurements, whereas satellite-based CRE estimates suggest a cooling effect. This discrepancy is primarily caused by a negative bias in the assumed surface albedo. Substantial biases are also identified for cloud height and low-level air temperature, but compensating effects and a relatively weak sensitivity of thermal-infrared radiation to these biases mitigate their impacts on the CRE.

1 Introduction

The Arctic is the hotspot of global warming and experiences a fast and immense transformation of its climate system (Walsh et al., 2011; Jeffries et al., 2013). Key indicators of this transition are the severe increase of the near-surface temperature, which is accelerated by a factor of two to four compared to the rest of the globe (Rantanen et al., 2022; Chylek et al., 2022; Wendisch et al., 2023), and the associated retreat of the Arctic sea ice. The annual minimum extent of sea ice in September has decreased by more than 40 % over the last 45 years (Meier et al., 2024), and a completely ice-free Arctic Ocean during summer is likely

https://doi.org/10.5194/egusphere-2026-2210
Preprint. Discussion started: 8 May 2026

to occur in the near future (Jahn et al., 2024; Heuzé and Jahn, 2024). However, several reanalysis products also suggest a deceleration of the Arctic warming and sea ice decline since 2012, especially during winter (Luo et al., 2025). Nevertheless, the sensitivity of the Arctic to global warming remains to be strong and further driven by a unique interplay of multiple processes and feedback mechanisms (Pithan and Mauritsen, 2014; Goosse et al., 2018), which intensify the initial warming and are commonly summarized as Arctic amplification (Serreze and Francis, 2006; Serreze and Barry, 2011; Wendisch et al., 2023). One of the important drivers contributing to Arctic amplification is the self-enforcing surface albedo feedback (Hall, 2004; Screen and Simmonds, 2010). The melting sea ice uncovers areas of darker, ice-free ocean surfaces, leading to increased absorption of solar radiation and, consequently, a warming of the upper ocean mixed layer. Once the heat from the mixed layer is released to the atmosphere, it amplifies the near-surface warming and sea ice melt and, thus, can modify the atmospheric circulation, which contributes to further changes of weather and climate in the Arctic and, probably, beyond in the mid-latitudes (Cohen et al., 2020; Crawford et al., 2022; Wendisch et al., 2024).

Due to the importance of sea ice as a main component of the Arctic climate system, it is crucial to understand the mechanisms triggering sea ice melt. The sea ice evolution is, besides ocean currents, largely controlled by advection of warm and moist airmasses from the south, cold airmasses from the central Arctic, and the local surface energy budget components, which comprise sensible, latent, conductive, and radiative energy fluxes. The surface radiation budget (SRB) is quantified by the net irradiance F^{net}, with:

$$F^{\mathrm{net}} = (F^{\downarrow}_{\mathrm{sol}} - F^{\uparrow}_{\mathrm{sol}}) + (F^{\downarrow}_{\mathrm{TIR}} - F^{\uparrow}_{\mathrm{TIR}}). \tag{1}$$

The terms containing $F^{\downarrow}$ and $F^{\uparrow}$ indicate the downward and upward irradiances (radiative energy flux densities) incident on and leaving the surface, respectively, both separated into components covering the solar (wavelength range of 0.3–4 µm, subscript "$_{\mathrm{sol}}$") and thermal-infrared (TIR, 4–100 µm, subscript "$_{\mathrm{TIR}}$") spectral ranges of atmospheric electro-magnetic radiation. Various modelling and observation-based studies suggest that the September sea ice extent is closely correlated to the SRB in spring and early summer, which modifies melt onset and melt rate (Kapsch et al., 2016; Huang et al., 2019). Therefore, monitoring and understanding the variability of the SRB as a function of air temperature, water vapor, surface albedo, and clouds is essential.

In particular, low-level clouds containing partly super-cooled liquid water, which frequently occur in the Arctic (Cesana et al., 2012), are a key factor that modifies the SRB. This modification is quantified by the cloud radiative effect (CRE), which is defined as the difference of the net irradiances in cloudy (all-sky, $F^{\mathrm{net}}_{\mathrm{cld}}$) and cloud-free ($F^{\mathrm{net}}_{\mathrm{cf}}$) conditions, with:

$$\mathrm{CRE} = F^{\mathrm{net}}_{\mathrm{cld}} - F^{\mathrm{net}}_{\mathrm{cf}}, \tag{2}$$

and likewise separable into a solar and a TIR component. Due to downward TIR radiation emitted by the relatively warm cloud base, clouds have a warming effect on the surface (positive CRE) in the TIR spectral range, while they cool the surface by reflecting radiation in the solar spectral range. Which of these two counteracting effects dominates and determines the sign of the total CRE, depends on the combined impacts of solar zenith angle (SZA), as well as surface, thermodynamic, and cloud conditions (Shupe and Intrieri, 2004). The TIR warming effect is often dominant for optically thin clouds, as they rapidly approach black body emission, while their reflectivity is still weak. Hence, these clouds are particularly predestinated to boost melt events, as, for example, observed over the Greenland ice sheet in July 2012 (Bennartz et al., 2013).

https://doi.org/10.5194/egusphere-2026-2210
Preprint. Discussion started: 8 May 2026

The most accurate information on the SRB and CRE are obtained from direct ground-based or low-level aircraft measurements of radiation as well as cloud and thermodynamic properties. Previous research exploited such observations to extensively investigate the variability of the SRB and the CRE with respect to seasonality, location, and their dependence on surface and atmospheric conditions (Shupe and Intrieri, 2004; Miller et al., 2015; Ebell et al., 2020; Becker et al., 2023, 2025). Although these investigations advanced the understanding of cloud–surface–radiation interactions, the data are limited to a few land-based locations or short-term field campaigns and do not provide persistent records representative for the entire Arctic. To achieve Arctic-wide, long-term monitoring of atmospheric and surface properties, observations from space-borne instruments onboard polar-orbiting satellites are indispensable. Due to the high revisiting frequency of such satellites in high latitude regions, these observations have the potential to complement the continuous ground-based and temporary campaign measurements with large spatial and temporal coverage. Unfortunately, direct satellite-based irradiance measurements are impossible, making the monitoring of the SRB from space challenging. Even at the top of the atmosphere (TOA), satellite-based observations of radiative flux densities require several assumptions. Measurements of the Clouds and the Earth's Radiant Energy System (CERES) instrument, installed on the satellites Terra, Aqua, Suomi-NPP, and NOAA20, only yield broadband TOA radiances within a solar (0.3–5 µm), a total (0.3–200 µm), and an atmospheric window (8–12 µm) channel (Loeb et al., 2018). The conversion of these initially measured radiances to irradiances involves scene-type-dependent angular distribution models, which are selected based on ancillary data of, i. a., cloud and surface properties (Su et al., 2015; Loeb et al., 2018).

To retrieve the radiation budget at the surface, various approaches are used, which rely on complementary products of atmospheric state parameters, including cloud properties, and surface albedo. Especially for the solar SRB component, some satellite products bypass an explicit cloud retrieval and apply pre-calculated regression models or look-up tables depending on water vapor amount and surface albedo to directly estimate the broadband surface irradiances from narrowband TOA radiance observations (Wang et al., 2020; Zhang et al., 2019; Karlsson et al., 2023; Liang et al., 2021). However, these products are usually restricted to land surfaces, provide TIR irradiances only partly, and are hardly available at a finer than daily temporal resolution. Other products, like the CERES Cloud Radiative Swath (CRS, Scott et al., 2022), explicitly simulate the radiation field using pixel-level satellite cloud products and assumptions on the surface albedo as input.

The CERES cloud product is based on atmosphere-corrected radiance measurements from the collocated Moderate-resolution Imaging Spectroradiometer (MODIS, onboard Terra and Aqua) and Visible Infrared Imaging Radiometer Suite (VIIRS, onboard Suomi-NPP and NOAA20) instruments. Cloud temperature, cloud optical thickness (COT), and cloud effective radius (CER) are derived from pre-simulated look-up tables covering radiances in the 11 µm, 3.75 µm, and 0.65 µm (or 1.2 µm over snow-covered surfaces) channels using an iterative procedure (Minnis et al., 2021). A similar approach is applied to measurements of the Multi-Spectral Imager aboard the newly launched EarthCARE satellite (Hünerbein et al., 2023). In contrast, the well-established cloud products MOD06/MYD06 from MODIS and CLDPROP from VIIRS obtain COT and CER based on the bispectral method proposed by Nakajima and King (1990). Depending on surface albedo and cloud thermodynamic phase, the microphysical cloud properties are inferred from look-up tables of the cloud top reflectance in non-absorbing (less than 1.2 µm) and weakly absorbing (between 1.6 µm and 3.7 µm) channels, which are predominantly sensitive to COT and CER, respectively (Platnick et al., 2017, 2020). However, retrieval uncertainties increase over highly reflecting snow and sea ice

https://doi.org/10.5194/egusphere-2026-2210
Preprint. Discussion started: 8 May 2026

surfaces in the Arctic due to the weak reflectance contrast between clouds and surface. Therefore, the application of a modified method, where the non-absorbing channel is replaced by the more strongly absorbing channel at 1.6 µm, is recommended over snow-covered surfaces (Platnick et al., 2001). Furthermore, several case studies by Chen et al. (2021) suggest that a significant amount of thin clouds seems to generally remain undetected by MODIS. Based on channel availability, the retrieval of cloud top height (CTH) differs between MOD06/MYD06 and CLDPROP. For mid- and high-level clouds, the former product applies the CO_2 slicing method to TOA radiances measured in channels between 13 µm and 15 µm, while the brightness temperature at 11 µm is used for low-level liquid water clouds (Baum et al., 2012). For VIIRS CLDPROP, where the CO_2 absorption bands are unavailable, the CTH is obtained from optimal estimation and the brightness temperatures measured in the 8.5 µm, 11 µm, and 12 µm channels (Heidinger and Pavolonis, 2009). However, both products require accurate atmospheric temperature and humidity profiles, which are usually taken from model analysis, for correct retrievals of the CTH, especially in the case of temperature inversions. Moreover, passive satellite imagers do not provide information on cloud base properties, such that the cloud base height (CBH) can only be estimated from statistical relationships with the COT that are usually based on comparisons with active remote sensing products (Noh et al., 2017; Minnis et al., 2021).

Accurate information on the surface albedo is not only crucial for precise SRB estimates, but also required to improve the quality of satellite cloud retrievals. Although numerous operational satellite products of surface albedo exist, none of them is perfectly suitable for radiative transfer calculations in the Arctic and the albedo used for cloud retrievals heavily relies on assumptions. The widely used kernel-based products MCD43 from MODIS and VNP43 from VIIRS retrieve spectral black-sky (direct) and white-sky (diffuse) surface albedo within the solar wavelength channels (Lucht et al., 2000), but perform poorly over snow-covered land surfaces and are unavailable over sea ice (Liu et al., 2017). In contrast, the products available over sea ice (e. g., the VIIRS Land Surface/Sea Ice Albedo product) only provide direct estimates of blue-sky (i. e., a linear combination of white-sky and black-sky albedo weighted by the diffuse fraction of $F_{\mathrm{sol}}^{\downarrow}$) broadband surface albedo (Peng et al., 2018; Qu et al., 2016), which refers to a specific SZA and can largely reduce the accuracy of $F_{\mathrm{sol}}^{\downarrow}$ in radiative transfer simulations. A general problem is that satellite-based retrievals of surface albedo work in cloud-free conditions only. However, given the relatively slow surface albedo change over time, most products fill cloudy pixels with values from previous observations under cloud-free conditions.

The multitude of challenges discussed above, which is further augmented by uncertainties of the ancillary thermodynamic profiles, limits the accuracy of SRB and CRE calculations from satellite observations and raises two questions that will be addressed in this paper: (i) How accurate are the satellite-derived cloud properties, the surface albedo used in the satellite cloud retrievals as well as ancillary thermodynamic profiles, and (ii) how do potential biases of these quantities affect the resulting SRB and CRE? Previous research by Chen et al. (2021) assessed the impact of MODIS-derived COT on the precision of simulated irradiances in the solar spectral range, performing a point-by-point comparison with aircraft irradiance measurements during two case studies in the Arctic. The present study complements this work by statistically comparing point-wise SRB and CRE simulations initialized with a set of satellite-derived quantities on the one hand, and collocated aircraft observations on the other hand, for an aggregation of cases over Arctic sea ice. The analysis includes solar and TIR irradiances and the satellite-derived input parameters are successively replaced by the aircraft-measured quantities to attribute the potential CRE bias to

https://doi.org/10.5194/egusphere-2026-2210
Preprint. Discussion started: 8 May 2026

discrepancies in cloud, thermodynamic, or surface properties. Section 2 introduces the aircraft measurements and satellite data and explains their use in the radiative transfer simulation. A comparison of satellite and aircraft observations and the simulated CRE resulting from different combinations of the input parameters are provided in Sects. 3 and 4, respectively. The CRE differences between satellite- and aircraft-based simulations are assessed separately for the solar and TIR spectral ranges and are then combined to examine the impact on the total surface CRE. Section 5 concludes the paper.

2 Measurements and methods

2.1 Campaign overview

The airborne measurements used in this study were collected during the Arctic Radiation-Cloud-Aerosol-Surface Interaction Experiment (ARCSIX), which operated out of Pituffik Space Base, Greenland (formerly known as Thule Air Base). The campaign aimed at investigating the impact of surface properties, clouds, and aerosol particles on the SRB and sea ice melt. To cover the melting season, ARCSIX was conducted in two phases between May and August 2024. The first phase took place during a three-week period in May/June and deployed the two aircraft P-3 Orion (P-3) and Gulfstream-III (G-III) operated by the United States National Aeronautics and Space Administration (NASA). During the second phase, lasting about three and a half weeks in July/August, a Learjet owned by the Stratton Park Engineering Company (SPEC Inc.) joined P-3 and G-III. Excluding transit flights, P-3, G-III, and Learjet performed 19, 13, and 10 measurement flights, respectively. The campaign dates and the flight statistics for both phases are given in Table 1; the flight tracks are illustrated in Fig. 1 together with the mean sea ice concentration. The majority of the research flights were designed such that a close coordination between the aircraft was achieved. The P-3 flew at low altitudes and performed in situ measurements of cloud, aerosol, and trace gas properties as well as spectral and broadband radiative quantities. Furthermore, a Raman lidar, a scanning polarimeter, and a laser altimeter for sea ice characterization were installed on the P-3. The Learjet supported the cloud observations of the P-3 with an equivalent set of in situ instruments and an additional cloud radar. The G-III was equipped with a spectral imager along with a lidar for remote sensing from high altitudes (11–12 km) and regularly launched dropsondes. Thus, the G-III built a bridge to space, with the ability to mimic observations from satellites. As the extensive validation of satellite-retrieved properties for advanced remote sensing algorithms and an improved long-term monitoring of the Arctic was an additional objective of ARCSIX, the aircraft flights were also closely coordinated with satellite observations. Further details on the instrumentation and flight operation are given in Taylor et al. (2026).

For studies of the CRE and the validation of satellite cloud products, specially designed cloud wall flight patterns were performed, which are highlighted in Fig. 1. A cloud wall consists of several stacked flight legs of 100–200 km length, which were performed by the P-3 to sample the atmosphere below, above, and inside a low-level cloud, typically in this order. To obtain information on the vertical structure of the cloud, a porpoise leg with alternating ascents and descents through the cloud layer along the wall was added. During three cloud wall maneuvers conducted during the second phase of ARCSIX, the Learjet was collocated to the P-3 and undertook the porpoise leg. As an example, the flight legs of the cloud wall performed on 7 June 2024 are illustrated in Fig. 2a. For 13 out of 15 cloud walls performed during ARCSIX, the G-III overpassed the P-3 and was

https://doi.org/10.5194/egusphere-2026-2210
Preprint. Discussion started: 8 May 2026

Table 1. Overview of the campaign phases and the corresponding flight statistics, excluding transit flights.

Period		P-3	G-III	Learjet
Phase 1 25 May–17 June	Flights	10	9	–
	(collocated)		(8)	
	Flight hours	68.0	45.6	–
Phase 2 22 July–16 August	Flights	9	4	10
	(collocated)		(4)	(4)
	Flight hours	68.0	21.1	34.8

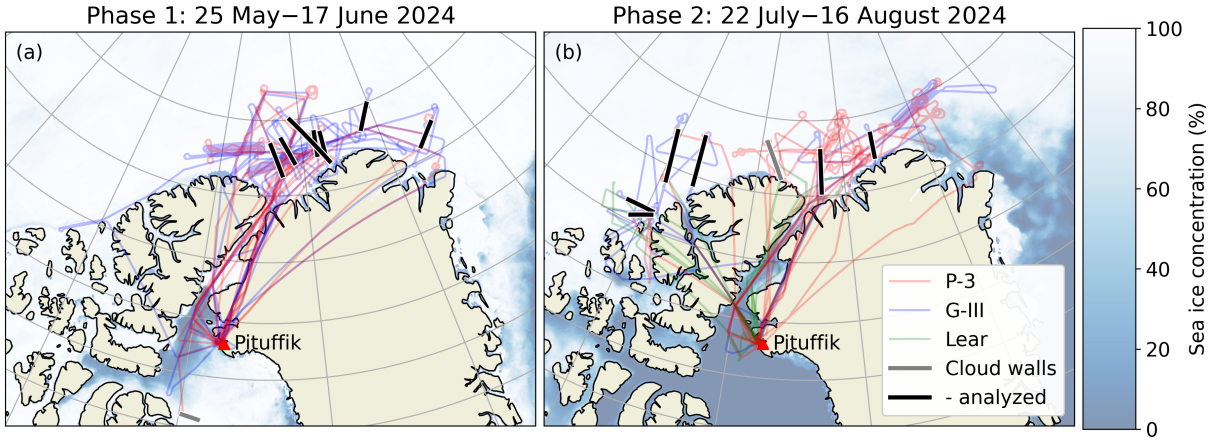

Figure 1. Flight tracks of all research flights during (a) the first phase and (b) the second phase of ARCSIX, color-coded by aircraft. Highlighted are the cloud walls used in the present analysis. The background shading shows the average sea ice concentration during the respective period.

collocated during at least one leg. Since the radiative transfer simulations require data of local thermodynamic profiles from dropsonde measurements, only these 13 cloud walls with a total length of 1534 km are included in the analysis (black lines in Fig. 1).

2.2 Data and setup of radiative transfer simulations

To determine their accuracy, satellite-derived cloud properties as well as ancillary data of thermodynamic profiles from meteorological analysis and surface albedo are collocated to corresponding aircraft observations for each point along the cloud walls (horizontal spacing of 110–130 m). The analyzed properties include the cloud microphysical quantities of liquid water path (LWP), ice water path (IWP), liquid water droplet effective radius (LER), and ice particle effective radius (IER), collectively referred to as CldMicro in the following; the cloud base and top heights (CldHeight); the vertical profiles of air temperature and humidity (TProf); and the surface albedo (Alb). For simplicity, the term satellite data also encompasses the ancillary data

https://doi.org/10.5194/egusphere-2026-2210
Preprint. Discussion started: 8 May 2026

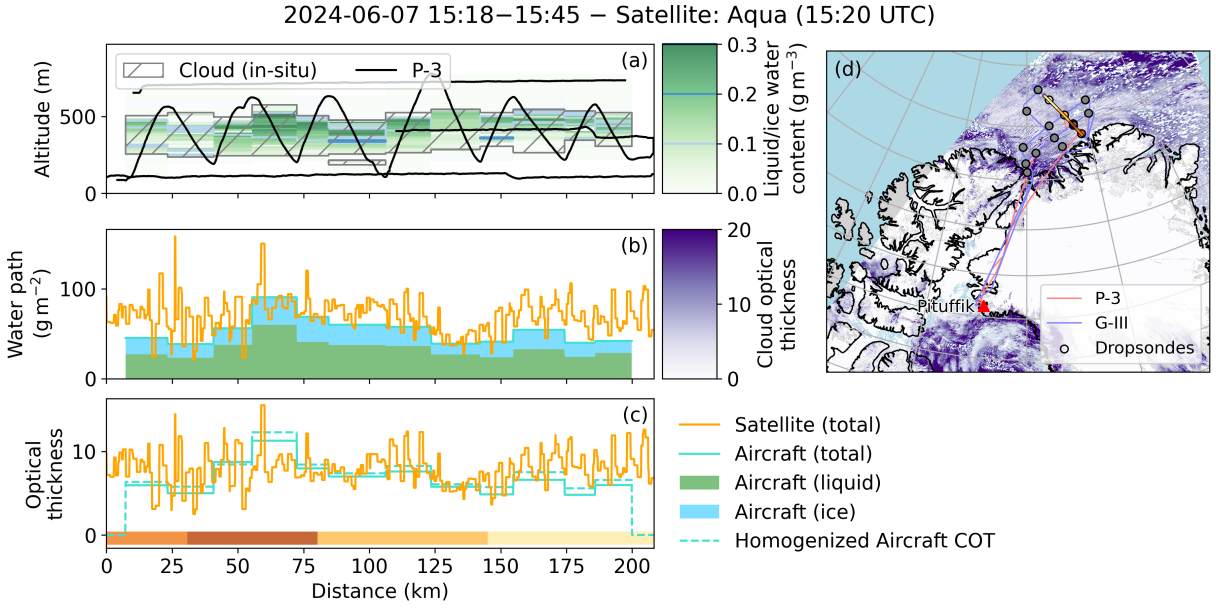

Figure 2. (a) Altitude of the flight legs performed along the cloud wall on 7 June 2024. The green shadings and blue contours illustrate profiles of LWC and IWC, respectively, which are derived from the measurements of in situ cloud probes during each ascent and descent of the porpoise leg. The consequent cloud boundaries are indicated by the gray frame and hatching. (b) Total CWP from aircraft and satellite observations, where the former is split into LWP and IWP calculated as the vertical integral of the LWC and IWC profiles shown in (a). (c) Total COT from aircraft and satellite observations as well as the homogenized aircraft-derived COT resulting from layer-constant effective radii. (d) Satellite COT of the granule collocated to the cloud wall. Additionally, the flight tracks of P-3 and G-III and the dropsonde locations are shown. Colored markers indicate dropsonde profiles used in the radiative transfer simulations for the data points marked by identical color of the highlighted cloud wall and at the bottom of (c).

in the following. The point-wise aircraft and satellite data are incorporated into radiative transfer simulations providing $F^{\downarrow}_{\mathrm{sol}}$, $F^{\uparrow}_{\mathrm{sol}}$, $F^{\downarrow}_{\mathrm{TIR}}$, and $F^{\uparrow}_{\mathrm{TIR}}$ in cloudy and cloud-free conditions to assess the uncertainty of the satellite-derived CRE. To detect the predominant sources of this uncertainty, the satellite data are successively replaced by the aircraft measurements. Table 2 gives an overview of the aircraft and satellite data used as simulation input. Details are specified in the remainder of this section. The aircraft-measured properties are regarded as ground truth in this study.

All simulations for the subsequent analysis are performed with the discrete ordinate solver (DISORT, Buras et al., 2011) of the radiative transfer code *uvspec*, which is included in the library for radiative transfer (libRadtran, Emde et al., 2016), and the results are output at surface level (0 m). For the solar simulations, the spectral range is 250–4000 nm and the molecular absorption is considered using the parameterization of Kato et al. (1999). The local SZA is calculated from time and position data provided by the aircraft during the below-cloud leg, while aerosol particle optical properties in the solar range are specified using the default profile representative for maritime clean environments (Hess et al., 1998). Simulations in the TIR range are run between 4 µm and 100 µm with the coarse molecular absorption parameterization by Gasteiger et al. (2014). The optical

https://doi.org/10.5194/egusphere-2026-2210
Preprint. Discussion started: 8 May 2026

Table 2. Overview of aircraft measurements and satellite/ancillary products used as input for the radiative transfer simulations.

		Aircraft	Satellite
CldMicro		liquid: FCDP ice: 2D-GRAY	MODIS MOD06/MYD06 VIIRS CLDPROP
CldHeight	CTH		
	CBH		statistical relationship based on CWP and CTH (Noh et al., 2017)
TProf		dropsondes	GEOS-FP
Alb		SSFR	statistical albedo (Moody et al., 2007) scaled with date-dependent melt parameterization and sea ice concentration

properties of the maritime clean aerosol profile do not cover the entire TIR wavelength range. However, since the simulated $F^{\downarrow}_{\mathrm{TIR}}$ in cloudy (cloud-free) conditions differs less than $0.1\,\mathrm{W\,m^{-2}}$ ($0.9\,\mathrm{W\,m^{-2}}$) between standard, rural aerosol conditions and a completely aerosol-free atmosphere, aerosol optical properties are neglected in the TIR simulations for simplicity.

2.2.1 Cloud properties

From an aircraft perspective, liquid and ice cloud properties are derived from measurements of the Fast Cloud Droplet Probe (FCDP) and the Two-Dimensional-Gray probe (2D-GRAY), respectively, which were installed on the P-3 and the Learjet among manifold other in situ cloud probes. The FCDP is a forward-scattering spectrometer probe measuring the number concentration and size distribution of spherical liquid cloud droplets in a diameter range of 1.5–50 µm with a resolution of 1.5–4 µm (Lawson et al., 2017). From the particle size distribution, liquid water content (LWC) and LER are calculated. The 2D-GRAY is an optical array probe used to determine the size of up to 1280 µm large particles with a resolution of 10 µm based on gray-scale images. Ice water content (IWC) and IER obtained from the size distribution of non-spherical particles by the method of Baker and Lawson (2006), are included in the data set. It is assumed, that no particles outside the size ranges of the instruments exist and that no liquid droplets are misinterpreted as ice and vice versa. Potential deviations from these assumptions are expected to only weakly alter the retrieved bulk microphysical properties. For every ascent and descent along the porpoise leg of each cloud wall, a tilted profile of LWC, LER, IWC, and IER through the cloud is obtained and projected onto a vertical axis. The resulting profiles are assumed constant over the entire horizontal extent of the respective ascent or descent, which is typically between 10 km and 20 km, but can reach up to 56 km in extreme cases. Although this horizontal resolution is rather coarse and results in a reduced variability compared to reality, only the porpoise sampling allows to fully characterize the vertical extent of the clouds. Figure 2a illustrates the vertical LWC and IWC profiles of a cloud reconstructed with the described method. Based on manually adjusted LWC and IWC thresholds, CTH and CBH are then derived from the microphysical profiles (gray frame and hatching in Fig. 2a): At least 20 m thick layers with either LWC or IWC of more than $0.025\,\mathrm{g\,m^{-3}}$ are considered cloudy and dry layers of less than 50 m are incorporated into the adjacent cloud layers. In the radiative transfer simulations for cloudy conditions, each resulting cloud layer is represented by the vertically integrated

https://doi.org/10.5194/egusphere-2026-2210
Preprint. Discussion started: 8 May 2026

LWP and IWP (Fig. 2b) as well as height-constant values of LER and IER, which are averages over the respective layer. This vertical homogenization of the cloud changes the COT compared to a fully resolved cloud profile (Fig. 2c) and leads to an underestimation (overestimation) of the simulated $F^{\downarrow}_{\mathrm{sol}}$ ($F^{\downarrow}_{\mathrm{TIR}}$) by on average 4.1 $\mathrm{W\,m^{-2}}$ (0.7 $\mathrm{W\,m^{-2}}$). Therefore, the average LER and IER are scaled to conserve the real liquid and ice optical thicknesses for each cloud layer in the solar spectral range, reducing the mean solar (TIR) bias to $-0.1\ \mathrm{W\,m^{-2}}$ (0.4 $\mathrm{W\,m^{-2}}$).

Space-borne cloud observations are obtained from the MODIS MOD06/MYD06 (Collection 6.1, Platnick et al., 2017) and VIIRS CLDPROP (Version 1.1, Platnick et al., 2020) cloud products. Despite different retrieval algorithms, both products provide pixel-level data of cloud phase and CTH as well as COT, CER, and cloud water path (CWP) at a spatial resolution of about 1 km and 0.75 km, respectively. The data are stored in consecutive granules, covering a period of five (MODIS) or six (VIIRS) minutes of observation. Considering the MODIS products from Terra (MOD06) and Aqua (MYD06), and the VIIRS products from Suomi-NPP and NOAA20, the granule temporally closest to the below-cloud leg and covering the cloud wall in its field of view is chosen to collocate the satellite observations to the aircraft measurements. Figure 2d shows the location of the example cloud wall (yellow-red line) and the COT from the corresponding satellite granule. Given the high frequency of polar-orbiting satellite overpasses in the Arctic, the maximum time difference between aircraft and satellite sampling is 45 minutes. Each data point along the cloud wall is then assigned the spatially closest satellite pixel for comparison. The satellite-derived CWP and COT collocated along the example cloud wall are shown in Figs. 2b and 2c, illustrating the horizontal resolution difference between satellite pixels and porpoise profiles. The microphysical properties are primarily taken from the snow-optimized version of the Nakajima and King (1990) retrieval (1.6–2.1 µm), but the standard product (1.2–2.1 µm) is used if the former is unavailable. As the general frequency of retrieval failures does not significantly differ between both products, these filled gaps comprise at maximum 9 % of the observations for individual cloud walls. For Aqua, measurements within the 1.6 µm channel are considered unreliable, such that the 1.2–2.1 µm retrieval is used throughout. However, a comparison of both retrievals for the other satellites indicates that the derived COT does not significantly differ statistically (on average 0.42, not shown). The CBH is not included in the cloud products and, therefore, determined based on Noh et al. (2017) using statistical correlations between CWP and cloud geometrical thickness. The radiative transfer simulations are then set up with CTH, CBH, CWP, and CER. Unlike for aircraft-measured cloud properties, where both phases can coexist, either liquid or ice clouds are included in the simulations based on the phase from the cloud retrieval. The mixed-phase clouds analyzed here are predominantly treated as liquid.

Since the effects of CldMicro and CldHeight are analyzed separately in this study, some simulations are set up with microphysical cloud properties from satellite and CBH and CTH from aircraft observations or vice versa. In the case of multi-layer clouds, which are generally not resolved by satellite observations, this configuration requires additional considerations. If CldHeight is derived from satellite and CldMicro from aircraft data, a single-layer cloud is simulated, where LWP and IWP correspond to the sum of all cloud layers and LER and IER are given by the total-column mean. Conversely, a satellite-derived CWP is partitioned among multiple cloud layers proportional to the aircraft-measured CWP distribution, while the CER is identical for all layers.

https://doi.org/10.5194/egusphere-2026-2210
Preprint. Discussion started: 8 May 2026

2.2.2 Thermodynamic profiles

Vertical profiles of measured air temperature and relative humidity are collected by dropsondes, which were typically launched at the edges of the cloud walls overflown by the G-III. Out of 139 dropsondes, 36 profiles were processed by the simulations. Each data point along the cloud wall is assigned the spatially closest dropsonde, resulting in a maximum distance of 71 km and a temporal difference of 100 minutes at most. For the example case, Fig. 2d shows the dropsonde locations and highlights the profiles corresponding to the identically colored segments of the wall, which are also indicated by the bar at the bottom of Fig. 2c. The 2 Hz measurements of the dropsondes resulted in a vertical resolution of 6–8 m below an altitude of 5 km. To improve the computational efficiency, the vertical resolution of the simulations was reduced such that only every 10th, 20th, and 40th level was included below 1 km, between 1 km and 2 km, and above 2 km, respectively. The surface skin temperature was measured by a downward-looking KT-19 infrared thermometer during the below-cloud leg.

Since thermodynamic profiles of air temperature and humidity are not obtained from satellite observations, ancillary data from the Goddard Earth Observing System forward processing product (GEOS-FP, version 5.29.5-p6) are used here. GEOS-FP provides three-hourly records of geometric height, air temperature, and relative humidity for 42 pressure levels (0.1–1000 hPa) as well as surface skin temperature and mean sea level pressure at a latitude–longitude resolution of 0.25° x 0.3125°. The data are spatially and temporally interpolated to the points of observation along the below-cloud leg of each wall. Thus, distinct profiles for each data point are included in the simulations with the vertical resolution given by GEOS-FP.

2.2.3 Surface albedo

Airborne observations of the spectral surface albedo are provided by the Spectral Surface Flux Radiometer system (SSFR) during the below-cloud leg. SSFR consists of an upward- and a downward-looking spectroradiometer, which measure spectral downward and upward irradiances, respectively, within a wavelength range of 350–2000 nm (Schmidt and Pilewskie, 2012). The spectral resolution is 6 nm below 950 nm and 12 nm for higher wavelengths, with a sampling resolution of 4 nm and 6 nm, respectively. To receive the downward irradiances on a horizontally aligned plane, the upward-looking sensor is stabilized by an active leveling platform, which compensates for aircraft attitude. From the ratio of upward to downward spectral irradiance, the spectral albedo is calculated in flight altitude (max. 340 m), but considered representative for the surface because the broadband albedo difference between both altitudes for the given conditions is well below 0.01 according to simplified radiative transfer simulations (not shown). Figure 3 shows the average surface albedo spectrum observed during the example cloud wall as a turquoise line. Due to the low signal-to-noise ratio in water vapor absorption bands, which can yield unrealistic surface albedo values and bias the radiative transfer simulations, surface albedo data in the ranges 1325–1430 nm and 1815–1970 nm (dark gray-shaded areas in Fig. 3) are not taken from the measurements but are linearly interpolated from the surrounding wavelengths. Furthermore, the solar wavelength ranges between 250 and 350 nm and between 2000 and 4000 nm (light gray-shaded areas in Fig. 3), which are not covered by SSFR, are set to the mean SSFR-measured spectral albedo in the range 350–400 nm and a constant 0.1, respectively. Since the spectral irradiances are generally low in these wavelength ranges, effects of this decision on the simulated broadband irradiances are weak. Note that the same spectral surface albedo is used for cloudy

https://doi.org/10.5194/egusphere-2026-2210
Preprint. Discussion started: 8 May 2026

and cloud-free simulations. Cloud-induced modifications of the spectral albedo are not corrected for, because their impact is difficult to quantify and would have induced additional uncertainties (Stapf et al., 2020). In some cases, thin, semi-transparent cloud layers were present below the aircraft, which altered the measured albedo, especially for wavelengths between 1400 nm and 1800 nm. Simplified radiative transfer simulations suggest that the distinct average albedo spectra of cases disturbed and not disturbed by these clouds cause differences in $F_{\mathrm{sol}}^{\uparrow}$ of less than 1 $\mathrm{W\,m^{-2}}$ within this wavelength range. Due to this weak effect, the data are not filtered for clouds below the aircraft. For the radiative transfer simulations, these surface-based clouds are assumed to not be present.

As operational satellite products providing spectral surface albedo over sea ice are not available, the pixel-level albedo data used by the cloud optical property retrievals of MOD06/MYD06 and CLDPROP, are also applied here. Over sea ice, this cloud-retrieval albedo is based on a simple five-year statistic of white-sky spectral albedo over permanently snow-covered surfaces derived from the MODIS MCD43 product (Moody et al., 2007), which is scaled with a rough melt parameterization that depends on the day of the year. The corresponding scaling factor is fixed to 0.8 during the summer months (June through August) and transitions from 1.0 to 0.8 during a 10-day period end of May. For pixels with mixed surface type coverage, the albedo additionally accounts for the sea ice concentration from the GEOS product for instrument teams (GEOS-IT). Over land surfaces, the operational MODIS MCD43 values are applied. Note that the granules containing the albedo information partly differ from those used for the cloud product, as VIIRS granules are not considered here. However, given the rather slow albedo changes within the time difference between the temporally closest MODIS and VIIRS observations, this granule difference does not pose a problem. In Fig. 3, the orange dots indicate the average spectral albedo along the example cloud wall for eight MODIS channels between 0.47 and 3.6 µm. To obtain a full and reasonably shaped spectrum of the surface albedo for the radiative transfer simulations, these channel values are combined with additional auxiliary points (triangles in Fig. 3) to quadratically interpolate the albedo values to the spectral resolution of SSFR (orange line in Fig. 3). The spectral shape of the albedo resulting from this quadratic interpolation resembles the shape of the SSFR-measured spectrum slightly better compared to a linear interpolation.

3 Statistical comparison of satellite and aircraft observations

The aircraft- and satellite-derived quantities described in Sect. 2.2 are aggregated for all cloud walls and analyzed statistically. To capture potential seasonal variations in satellite retrieval performance, separate analyses are presented for the two campaign phases. Although the cloud walls captured a wide range of atmospheric conditions over Arctic sea ice, their statistical representativeness for the Arctic ocean is still limited by the flight strategy and the number of samples considered in this study. As the flight activities were concentrated over ice-covered ocean surfaces, analyses over open ocean are not provided here.

3.1 Microphysical cloud properties

Figure 4 displays histograms of aircraft- and satellite-derived CWP and COT. For the aircraft measurements, both quantities are obtained as the sum of liquid and ice cloud properties. During the first phase of ARCSIX (Fig. 4a), almost two thirds

https://doi.org/10.5194/egusphere-2026-2210
Preprint. Discussion started: 8 May 2026

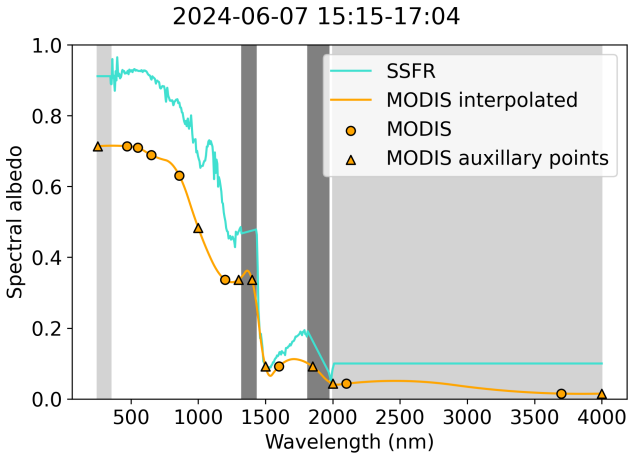

Figure 3. Spectrum of SSFR-measured surface albedo averaged for the cloud wall on 7 June 2024. The mean albedo values used by the satellite cloud retrievals and a number of auxiliary points are indicated by the symbols and used to quadratically interpolate albedo values to the SSFR wavelengths between the MODIS channels.

of the clouds exhibited a CWP between 20 $\mathrm{g\,m^{-2}}$ and 80 $\mathrm{g\,m^{-2}}$, whereas larger values occurred only occasionally. Optically thin clouds, which are sensitive to the TIR emissivity and typically defined by a CWP below 30 $\mathrm{g\,m^{-2}}$ (black dotted line), account for about 20 % of the aircraft observations. The median CWP is 56 $\mathrm{g\,m^{-2}}$. The MODIS and VIIRS retrievals mostly overestimate the CWP during the first phase, yielding a median of 81 $\mathrm{g\,m^{-2}}$ and a reduced fraction of optically thin clouds, which is only about 5 %.

The second phase of ARCSIX was characterized by optically thicker clouds (Fig. 4b). The aircraft measurements indicate that the CWP was almost constantly larger than 70 $\mathrm{g\,m^{-2}}$, with a median of 180 $\mathrm{g\,m^{-2}}$, while optically thin clouds occurred for less than 2 % of the data points. The coarse horizontal resolution of the porpoise ascents and descents leads to a relatively low number of unique CWP values, preventing a smoother appearance of the aircraft-measured CWP histogram in Fig. 4b. However, the statistical underestimation of the CWP by the satellite observations for the cases analyzed here is likely not linked to this limited sampling resolution. Although the fractions of optically thin clouds are comparable for aircraft and satellite observations, the median satellite-derived CWP is only 104 $\mathrm{g\,m^{-2}}$. In contrast to the aircraft measurements, the satellite-derived frequency distributions are rather similar between both campaign phases and do not capture the observed variability.

Figures 4c and 4d illustrate the corresponding histograms of the COT, which is more directly related to $F_{\mathrm{sol}}^{\downarrow}$ than the CWP. Note that the COT is wavelength-dependent, but approximately constant across the solar spectral range. The overall shapes of the distributions resemble those of the CWP, reflecting the relatively weak variability of the CER that links CWP to COT. The interquartile range (IQR) of the satellite-retrieved CER spans from 10.5 µm to 14.5 µm. Although this range does not match either LER (IQR 8.3–10.0 µm) or IER (IQR 25.5–31.0 µm) derived from the in situ probes, it is representative for the effective radius of the combined liquid–ice particle size distribution, which reveals an IQR of 10.7–12.7 µm. The resulting median COT

https://doi.org/10.5194/egusphere-2026-2210
Preprint. Discussion started: 8 May 2026

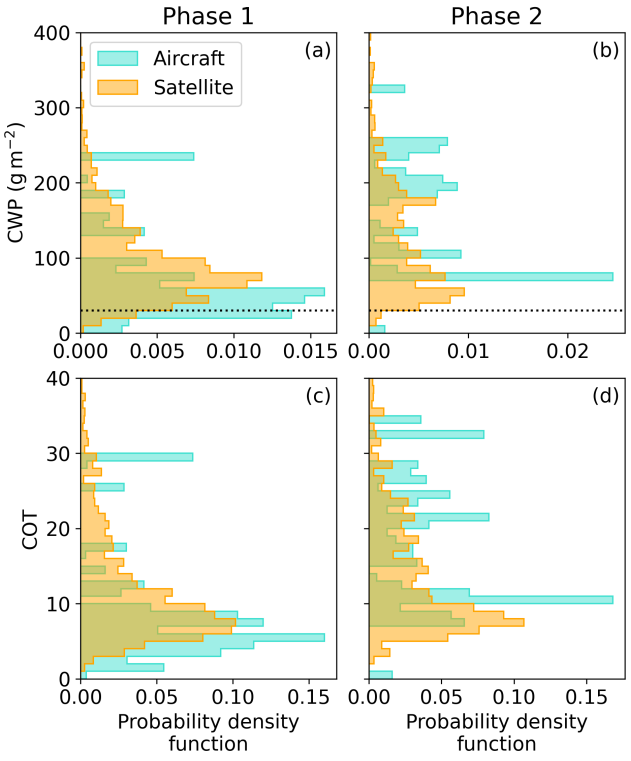

Figure 4. Probability density functions of aircraft-measured and satellite-derived (a,b) CWP and (c,d) COT, separated for (a,c) the first and (b,d) the second phase of ARCSIX. The dotted line in (a) and (b) indicates the CWP threshold of 30 g m^{-2}, discriminating optically thin and thick cloud regimes.

values are 7.0 and 9.6 during the first phase, and 17.2 and 11.7 during the second phase of ARCSIX for the aircraft and satellite observations, respectively.

In general, weak correlations are found between aircraft- and satellite-derived COT, indicating that the differences between the two are largely unsystematic. The coefficient of determination R^2 reaches 0.29 at most for individual cloud walls and decreases to 0.06 considering all observations. Partly, this weak correlation may be explained by the differences in spatial resolution between aircraft and satellite observations. However, R^2 improves only marginally to 0.09 when the resolution of the satellite data is coarsened to that of the porpoise profiles. Moreover, temporal mismatches between the observations could contribute to the discrepancies, but the data show no evidence that the correlation between aircraft- and satellite-derived COT increases for decreasing temporal difference. Further possible reasons contributing to the weak agreement include deficiencies of the satellite cloud retrievals in the Arctic, measurement uncertainties of the in situ cloud probes, and the assumptions made for cloud reconstruction (Sect. 2.2.1). Unlike for Chen et al. (2021), neither the detection of thin clouds nor the success rate of the cloud retrieval poses a major problem in this study. The reason for the overall good cloud detection is that the flight

https://doi.org/10.5194/egusphere-2026-2210
Preprint. Discussion started: 8 May 2026

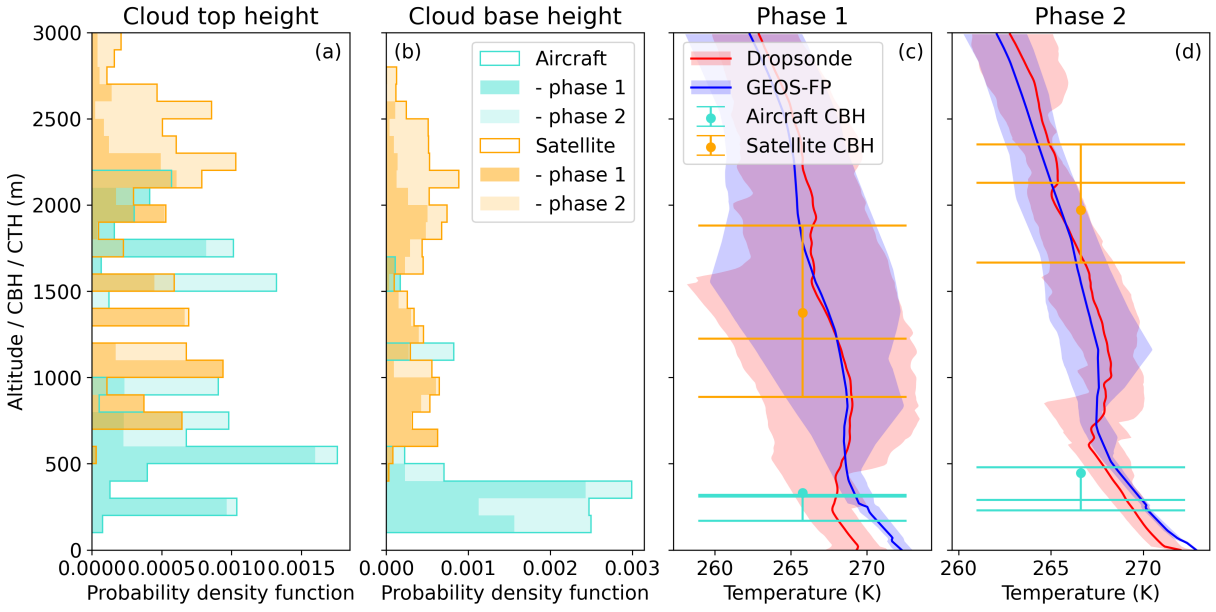

Figure 5. (a) Probability density function of aircraft-measured and satellite-derived (a) CTH and (b) CBH, separated for both campaign phases. Mean temperature profiles (lines) together with the corresponding interquartile-range (shadings) obtained from dropsondes and GEOS-FP for (c) the first and (d) the second phase of ARCSIX. The dots and horizontal lines in (c) and (d) indicate the phase-separated CBH statistics (mean as well as 25th, 50th, and 75th percentile).

activities specifically targeted clouds that were clearly visible in satellite imagery. Retrieval failures, which rarely coincide with actual thin clouds according to the in situ measurements, occur scarcely and are excluded from the subsequent analysis.

3.2 Cloud height and thermodynamic profile

Histograms of the satellite-derived and the highest aircraft-observed CTH are illustrated in Fig. 5a. During both phases of ARCSIX, in total 60 % of the clouds sampled by the in situ cloud probes, mostly single-layer, revealed CTHs below 1000 m, with a median of 570 m. The remaining observations form a second mode between 1400 m and 2200 m and are predominantly associated with multi-layer cloud regimes. The overall CTH median is 540 m during the first and 1460 m during the second campaign phase. The satellite observations likewise exhibit two distinct modes, which are shifted towards higher CTH values compared to the in situ measurements. However, unlike for the aircraft observations, these modes separate the MODIS and VIIRS data rather than single- and multi-layer cloud regimes, and reveal median values of 1150 m and 2360 m, respectively. These systematic differences highlight the inconsistencies among the cloud height retrieval algorithms and emphasize the difficulty of retrieving the height of Arctic low-level clouds from space. Overall, the satellite-derived CTH is overestimated for 83 % of the data points, with a mean bias of 740 m.

https://doi.org/10.5194/egusphere-2026-2210
Preprint. Discussion started: 8 May 2026

Figure 5b displays the probability density functions of the CBH and indicates that the sampled cloud systems were dominated by low-level clouds even if higher cloud layers were present. During both campaign phases, more than 80 % of the clouds revealed a CBH of less than 600 m, with median values of 310 m and 290 m for the first and second phase, respectively. The remaining cloud bases were observed between 1120 m and 1610 m. As for the CTH, the distribution of the satellite-derived CBH is comprised of two well-separated modes corresponding to MODIS and VIIRS observations. Nearly all retrieved CBH values exceed 600 m and extend up to 2770 m, resulting in median values of 1225 m for the first and 2128 m for the second phase of ARCSIX . Although the CBH is not directly retrieved by the MODIS and VIIRS cloud algorithms, these numbers suggest that the positive CTH bias propagates into CBH estimates. Only to a smaller extent contributes a negative bias in cloud geometrical thickness (on average 84 m for single-layer clouds), which is statistically related to the CWP (Noh et al., 2017), to the CBH overestimation. This negative bias occurs despite the frequently high-biased satellite CWP.

In the TIR spectral range, cloud height strongly determines the surface CRE in conjunction with the concurrent thermodynamic profiles of air temperature and humidity. Figures 5c and 5d show the mean temperature profiles from dropsondes and GEOS-FP for the first and second phase of ARCSIX, respectively. Additionally, simplified CBH statistics are provided for an estimate of the cloud base temperature (CBT). During the first phase of ARCSIX (Fig. 5c), GEOS-FP overestimated the air temperature below 500 m by approximately 2–3 K, yielding a mean surface temperature of −0.9 °C compared to −3.9 °C measured by the dropsondes. In higher altitudes, a slightly negative bias of less than 1 K is evident, but the overall agreement between the mean temperature profiles and their IQRs (shaded areas) is good. Consequently, GEOS-FP exhibits a weaker temperature inversion at the boundary layer top. Given the relatively low variability in aircraft-measured CBH, the CBT obtained in combination with the dropsonde profiles ranges between −10 °C and −1 °C, with a median of −4.9 °C. In contrast, the larger variability in satellite-derived CBH and GEOS-FP temperature results in a broader CBT range of −13–2 °C. However, due to the inversion in-between, the associated median CBT value is only about 1 K lower compared to the actual CBT.

The second phase of ARCSIX (Fig. 5d) exhibits a similar behaviour as the first phase: Below 700 m, GEOS-FP shows a higher temperature compared to the dropsondes and a slightly lower temperature aloft. However, this near-surface warm bias is significantly weaker than during the first phase, leading to a smaller difference in mean surface temperatures between dropsondes (−1.1 °C) and GEOS-FP (−0.3 °C). Furthermore, the general temperature variability represented by the IQR is reduced. Although the second phase was later in summer, only the lowest altitudes reveal warmer temperatures compared to the first phase, while the free troposphere was colder. This pattern is also reflected in the CBTs, which show median (min./max.) values of −5.1 °C (−8 °C/−2 °C) for the aircraft measurements and −7.9 °C (−12 °C/−1 °C) for the combination of satellite CBH and GEOS-FP temperature profile. Note also that the higher satellite CBH during the second phase is primarily linked to a higher frequency of VIIRS observations.

In addition to temperature, the TIR CRE is affected by the water vapor content below the cloud. The profiles of absolute humidity, which are not shown here, exhibit characteristics similar to those of the temperature. During the first phase, the warm bias of GEOS-FP in the lowest altitudes coincides with higher absolute humidity. Above the boundary layer, and generally throughout the second phase, the agreement between the averaged dropsonde and GEOS-FP profiles is strong.

https://doi.org/10.5194/egusphere-2026-2210
Preprint. Discussion started: 8 May 2026

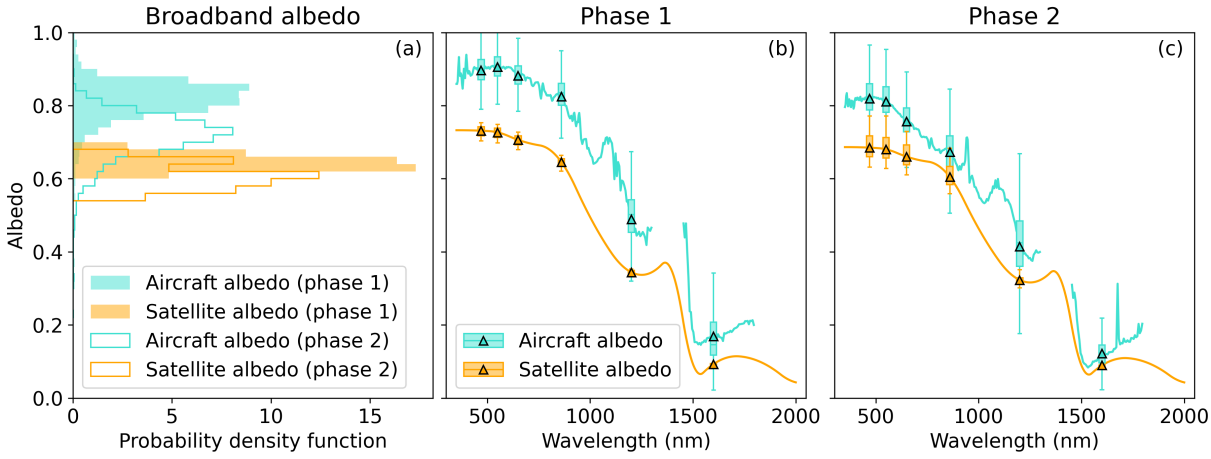

Figure 6. (a) Probability density function of broadband surface albedo derived from aircraft measurements and assumed for the satellite cloud retrievals, separated for both campaign phases. Mean aircraft-measured and cloud-retrieval albedo spectra (lines) and spectral albedo statistics at six wavelengths covered by MODIS channels (boxplots) for (b) the first and (c) the second phase of ARCSIX.

3.3 Surface albedo

Statistics of the surface albedo for the two phases of ARCSIX are displayed in Fig. 6. Figure 6a shows histograms of the broadband surface albedo, which is calculated from spectrally integrating the albedo either measured by SSFR or assumed for the satellite cloud retrievals, weighted by the spectral downward irradiance from SSFR. Note that the broadband albedo shown here refers to the spectral range covered by SSFR only. The contributions of wavelengths outside this range will scarcely alter the broadband albedo. During the first campaign phase, the aircraft observations over mostly snow-covered sea ice reveal a relatively broad distribution of broadband albedo values, ranging from 0.7 to 1.0 and generating a median of 0.82. In contrast, the cloud-retrieval broadband albedo substantially underestimates the ground truth, resulting in a median value of 0.64 only. This underestimation is largely linked to the scaling applied to account for the sea ice melt. Descaling the data yields a median of 0.79 for the broadband albedo. Moreover, due to the coarser spatial resolution and the limited variability in GEOS-IT sea ice concentration (92–100 %), this ancillary data is not able to capture small-scale variability in surface albedo, which explains the narrower range of the corresponding albedo distribution. Statistics of the spectral albedo for the wavelengths of the MODIS channels and the mean spectra of aircraft-derived and cloud-retrieval surface albedo for the first phase of ARCSIX are resolved in Fig. 6b. The boxplots confirm the lower values, especially in the visible range, and the weaker variability of the surface albedo used in the cloud retrievals.

During the second phase of ARCSIX, both the aircraft-derived and the cloud-retrieval broadband surface albedo are lower than during the first phase (Fig. 6a), with respective median values of 0.72 and 0.60. Airborne camera imagery demonstrates that this seasonal surface albedo decrease is related to larger open water areas and the formation of melt ponds (not shown). However, the cloud-retrieval albedo only accounts for the former effect, as the impact of the melt parameterization is nearly

https://doi.org/10.5194/egusphere-2026-2210
Preprint. Discussion started: 8 May 2026

identical for both campaign phases. Consequently, the difference between aircraft-derived and cloud-retrieval albedo is slightly smaller during the second phase. Omitting the albedo scaling would increase the median broadband albedo to 0.75, indicating that the current assumptions for sea ice melt are still too extreme, but also that accounting for this effect is necessary. The width of the albedo distributions is larger compared to the first phase, which is supported by the boxplots of the spectral albedo in Fig. 6c. This higher variability is especially evident for the cloud-retrieval surface albedo and related to the broader range of GEOS-IT sea ice concentration between 82 % and 97 %.

In summary, the discrepancy in surface albedo between aircraft observations and assumptions for the satellite cloud retrievals is largely related to the scaling of the statistical albedo to account for sea ice melt. The impact of melt is overestimated, leading to a low bias in surface albedo during Arctic summer, which is actually a wide-spread problem in modelling and satellite remote sensing. Huang et al. (2022) found that the CERES albedo similarly underestimates measurements performed during the Multidisciplinary drifting Observatory for the Study of Arctic Climate (MOSAiC). Furthermore, the multi-model mean surface albedo of the Coupled Model Intercomparison Project Phase 6 (CMIP6) collection tends to be even lower than the CERES albedo in the summertime Central Arctic, indicating the weak albedo representation in many climate models (Kim and Taylor, 2026). These results emphasize the difficulty of accurately representing, i. a., sea ice melt and melt pond formation in albedo parameterizations as well as the need for advanced representation of snow and sea ice albedo in climate models and satellite retrievals. The albedo measurements and further observations performed during ARCSIX have the potential to serve as a starting point for this improvement.

4 Impact of satellite observation uncertainties on the cloud radiative effect

4.1 Thermal-infrared irradiances

In the TIR spectral range, the CRE at the surface is mainly influenced by the microphysical cloud properties and the interplay of cloud height and thermodynamic profile. Prior to statistically quantifying the simulated TIR irradiances for different combinations of these either satellite- or aircraft-derived input parameters, the impact of their differences between satellite and aircraft observations on $F^{\downarrow}_{\mathrm{TIR}}$ is analyzed.

4.1.1 Impact of microphysical cloud properties

The difference in simulated $F^{\downarrow}_{\mathrm{TIR}}$ (aircraft minus satellite input) resulting from the discrepancy in CldMicro is illustrated in Fig. 7 for each individual data point as a function of aircraft- and satellite-derived CWPs. The remaining input parameters are obtained from the satellite data for both simulation setups. The figure shows that $F^{\downarrow}_{\mathrm{TIR}}$ is sensitive to a CWP difference only if one of the CWP values is lower than the threshold of $30\,\mathrm{g\,m^{-2}}$ separating optically thin and thick clouds (dotted lines). If both values exceed this threshold, the $F^{\downarrow}_{\mathrm{TIR}}$ difference is negligible, independent of CWP discrepancy. This saturation effect is a typical feature of TIR radiation emitted by optically thick clouds, as their emissivity approaches unity (black body emission) around the specified CWP threshold (Shupe and Intrieri, 2004). Optically thick clouds were identified for the vast majority of

https://doi.org/10.5194/egusphere-2026-2210
Preprint. Discussion started: 8 May 2026

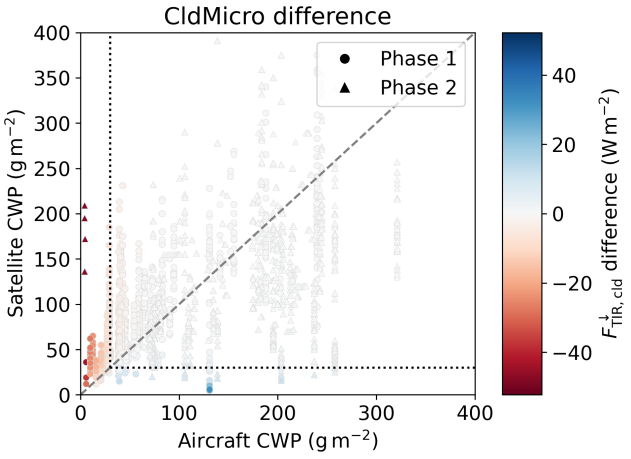

Figure 7. Aircraft- versus satellite-derived CWP, separated for the first (dots) and second (triangles) phase of ARCSIX. The color-coding indicates the difference between $F^{\downarrow}_{\mathrm{TIR}}$ in cloudy conditions resulting from simulations with satellite- and aircraft-derived input for CldMicro (aircraft minus satellite), while the remaining input parameters are taken from satellite observations. The black dotted lines mark the threshold of 30 g m^{-2} used to separate optically thin and thick clouds.

data points. Especially for the second phase of ARCSIX, Fig. 7 indicates a low number of optically thin clouds observations. However, for these few cases, the values of $F^{\downarrow}_{\mathrm{TIR}}$ obtained with the satellite-derived CWP significantly overestimated the values resulting from the aircraft-derived CWP by roughly 50 W m^{-2}. During the first campaign phase, a larger collection of thin cloud observations was classified as optically thick by the satellite retrievals, causing an enhanced $F^{\downarrow}_{\mathrm{TIR}}$ compared to the simulations with aircraft-measured cloud properties.

4.1.2 Impact of cloud height and thermodynamic profile

The impacts of CldHeight and TProf on $F^{\downarrow}_{\mathrm{TIR}}$ are closely linked, as the CBT largely determines the radiation emitted by the cloud base towards the surface. The differences in CBT and simulated $F^{\downarrow}_{\mathrm{TIR}}$ (aircraft minus satellite input) resulting from the distinct CldHeight between satellite and aircraft cloud observations are shown in Fig. 8a (blue symbols). The simulation input for CldMicro and TProf is fixed to the satellite cloud product and GEOS-FP, respectively, for this comparison. In accordance with the increase of the GEOS-FP temperature towards the surface (Fig. 5), the majority of data points during both campaign phases reveals a warmer CBT at the lower, aircraft-measured CBH (positive CBT difference), which causes a larger $F^{\downarrow}_{\mathrm{TIR}}$ at the surface. Although TIR irradiances are proportional to the air temperature to the fourth power, the data generally suggest a nearly linear increase of $F^{\downarrow}_{\mathrm{TIR}}$ with increasing CBT within the temperature range analyzed here. Despite the respectable correlation ($R^2 = 0.89$), the resulting surface $F^{\downarrow}_{\mathrm{TIR}}$ difference is significantly weaker than the emission difference expected from the CBTs, assuming black body emission (green symbols in Fig. 8a). The distinct slopes imply the impact of non-uniform atmospheric water vapor absorption and reemission below the cloud on the $F^{\downarrow}_{\mathrm{TIR}}$ difference. Although the thermodynamic profile is identical in both cases (GEOS-FP), the vertical extent of the atmospheric column, and, thus, the integrated water vapor (IWV) below

https://doi.org/10.5194/egusphere-2026-2210
Preprint. Discussion started: 8 May 2026

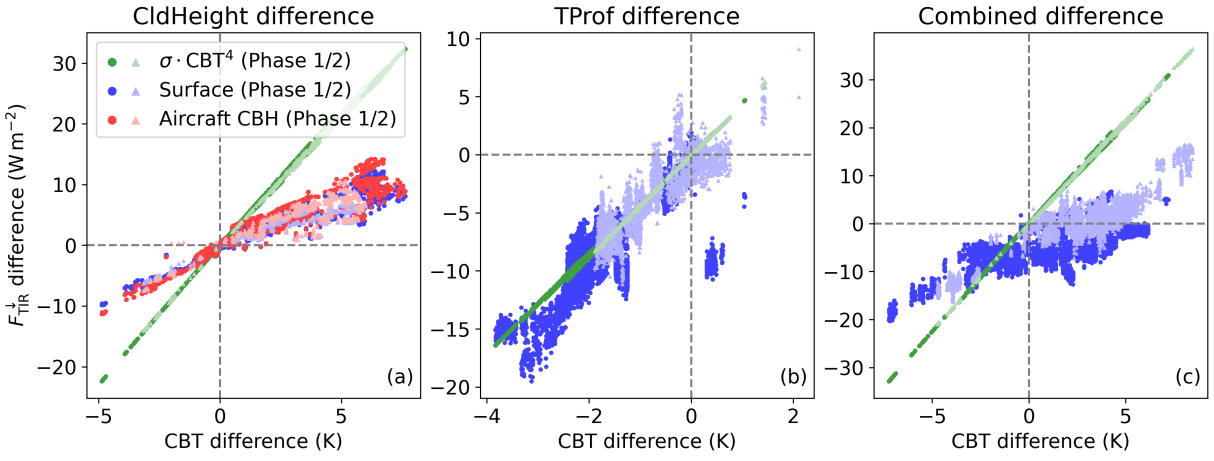

Figure 8. Difference in CBT and $F^{\downarrow}_{\mathrm{TIR}}$ in cloudy conditions, separated for the first (dark-colored dots) and the second (light-colored triangles) phase of ARCSIX and resulting from simulations with (a) satellite- and aircraft-derived CldHeight (aircraft minus satellite), (b) distinct input for TProf (dropsondes minus GEOS-FP), and (c) the combined change of CldHeight and TProf. The blue symbols represent the irradiance difference at the surface, the green symbols mark the theoretical black body emission at the cloud base, and the red symbols indicate the irradiance difference just below the aircraft-measured CBH.

the cloud are reduced when the satellite-derived CBH is replaced by the aircraft measurements. The on average $3.2\,\mathrm{kg\,m^{-2}}$ lower IWV decreases the absorbed portion of the cloud-emitted irradiance that is reemitted at usually warmer atmospheric temperature below the cloud and, therefore, limits the increase of $F^{\downarrow}_{\mathrm{TIR}}$ towards the surface. In combination with the warmer aircraft-derived CBT, this reduced $F^{\downarrow}_{\mathrm{TIR}}$ increase causes that the surface $F^{\downarrow}_{\mathrm{TIR}}$ difference is smaller compared to the cloud-emitted irradiance difference for the given aircraft–satellite CBH contrast. The red symbols in Fig. 8a represent the irradiance difference just below the aircraft-derived CBH. The good agreement with the $F^{\downarrow}_{\mathrm{TIR}}$ difference at the surface demonstrates that the additional water vapor between satellite- and aircraft-derived CBH largely accounts for the modification of the relationship between CBT difference and $F^{\downarrow}_{\mathrm{TIR}}$ difference.

Modifying TProf similarly results in changes of CBT as well as temperature and humidity characteristics below the cloud. Figure 8b shows the same analysis as Fig. 8a, but for the differences between simulations initialized with dropsonde-measured and GEOS-FP profiles. For these simulations, CldMicro is obtained from satellite observations and CldHeight corresponds to aircraft measurements. In contrast to Fig. 8a, most data points reveal negative and absolutely larger $F^{\downarrow}_{\mathrm{TIR}}$ differences, corresponding to the lower air temperature obtained from the dropsondes compared to GEOS-FP at the aircraft-derived CBH (Fig. 5). Especially for the first phase of ARCSIX, CBT differences of down to $-4\,\mathrm{K}$ are found, while the more similar temperature profiles during the second phase inhibit differences lower than $-2\,\mathrm{K}$. Compared to Fig. 8a, the slopes of the differences in surface $F^{\downarrow}_{\mathrm{TIR}}$ and cloud-emitted irradiance show better agreement, which implies that the atmospheric impact below the cloud differs weakly. Despite a significant overestimation of low-level absolute humidity by GEOS-FP, especially

https://doi.org/10.5194/egusphere-2026-2210
Preprint. Discussion started: 8 May 2026

during the first campaign phase, the impact of water vapor is restricted by the generally small distance between the low-level cloud and the surface. The IWV differences are one order of magnitude smaller compared to Fig. 8a.

The distinct importance of water vapor for the effects of CldHeight and TProf distorts the relationship between the differences in $F^{\downarrow}_{\mathrm{TIR}}$ and CBT when both effects are combined (Fig. 8c). While a CBT change of 1 K induced by the effect of TProf is associated with a $F^{\downarrow}_{\mathrm{TIR}}$ difference of more than 4 $\mathrm{W\,m^{-2}}$ (Fig. 8b), the below-cloud IWV difference resulting from the distinct CldHeight partly offsets a difference in cloud-emitted irradiance and causes a surface $F^{\downarrow}_{\mathrm{TIR}}$ difference of roughly 1.3 $\mathrm{W\,m^{-2}}$ per Kelvin only (Fig. 8a). Thus, the decreasing effect of TProf on $F^{\downarrow}_{\mathrm{TIR}}$ dominates over the increasing effect of CldHeight for similar CBT differences, which are frequent especially during the first phase of ARCSIX. However, this rough compensation of CBT differences does not coincide with a full compensation in $F^{\downarrow}_{\mathrm{TIR}}$. In fact, for numerous data points, the CBT obtained from aircraft measurements and dropsonde profiles is larger than the satellite- and GEOS-derived CBT (positive CBT difference), but the corresponding $F^{\downarrow}_{\mathrm{TIR}}$ difference is negative. Nevertheless, the $F^{\downarrow}_{\mathrm{TIR}}$ difference tends to increase for larger CBT difference.

4.1.3 Statistical simulation results

To statistically quantify the individual contributions of the previously discussed effects on the TIR irradiances, Fig. 9 compares the simulation results under cloudy and cloud-free conditions for different combinations of satellite- and aircraft-derived input parameters. In all panels, the leftmost (gray) boxplot represents the simulations based solely on satellite (and ancillary) data, while the rightmost (red) boxplot results from pure aircraft-measured input and is considered ground truth. In-between, the results for several configurations with satellite-derived input partially replaced by the aircraft measurements are given to isolate the impacts of the individual drivers.

The simulation results of $F^{\downarrow}_{\mathrm{TIR}}$ in cloudy conditions are displayed in Fig. 9a for the first phase of ARCSIX. The simulations with satellite-only input (labeled "None") yield a median of 298 $\mathrm{W\,m^{-2}}$, with the central 50 % of data lying in a range between 288 $\mathrm{W\,m^{-2}}$ and 304 $\mathrm{W\,m^{-2}}$. On the other hand, the median representing the ground truth ("TProf + CldHeight + CldMicro" from aircraft measurements) amounts to only 288 $\mathrm{W\,m^{-2}}$. Although this decrease in $F^{\downarrow}_{\mathrm{TIR}}$ seems counterintuitive given the high-biased satellite-derived CBH, it reflects compensating effects of CldHeight and TProf and is consistent with the occasional misclassification of optically thin clouds as optically thick by the satellite retrievals (Fig. 7). Consequently, replacing only CldMicro with aircraft measurements (labeled "CldMicro") reduces the median $F^{\downarrow}_{\mathrm{TIR}}$ to 289 $\mathrm{W\,m^{-2}}$. The magnitude of this decline is statistically limited by the relatively small number of misclassified data points. Consistent with the CBH difference, an additional change in CldHeight from satellite to aircraft observations increases the median of the surface $F^{\downarrow}_{\mathrm{TIR}}$ by about 9 $\mathrm{W\,m^{-2}}$ ("CldHeight + CldMicro"), which is less than expected from the CBT contrast (about 12 $\mathrm{W\,m^{-2}}$) due to the simultaneously reduced vertical extent of the below-cloud layer (Fig. 8a). The narrower range of aircraft-measured CBT raises the lower IQR bound of $F^{\downarrow}_{\mathrm{TIR}}$ compared to using the satellite-retrieved CldHeight. The counteracting effect of changing TProf from GEOS-FP to dropsonde profiles, causing colder temperatures at the aircraft-measured CBH (Fig. 5b), reduces the median $F^{\downarrow}_{\mathrm{TIR}}$ by 10 $\mathrm{W\,m^{-2}}$, which indicates that the effect of TProf slightly overcompensates the effect of CldHeight. Although the median CBT resulting from the combination of satellite-derived CBH and GEOS-FP temperature is slightly lower compared to

https://doi.org/10.5194/egusphere-2026-2210
Preprint. Discussion started: 8 May 2026

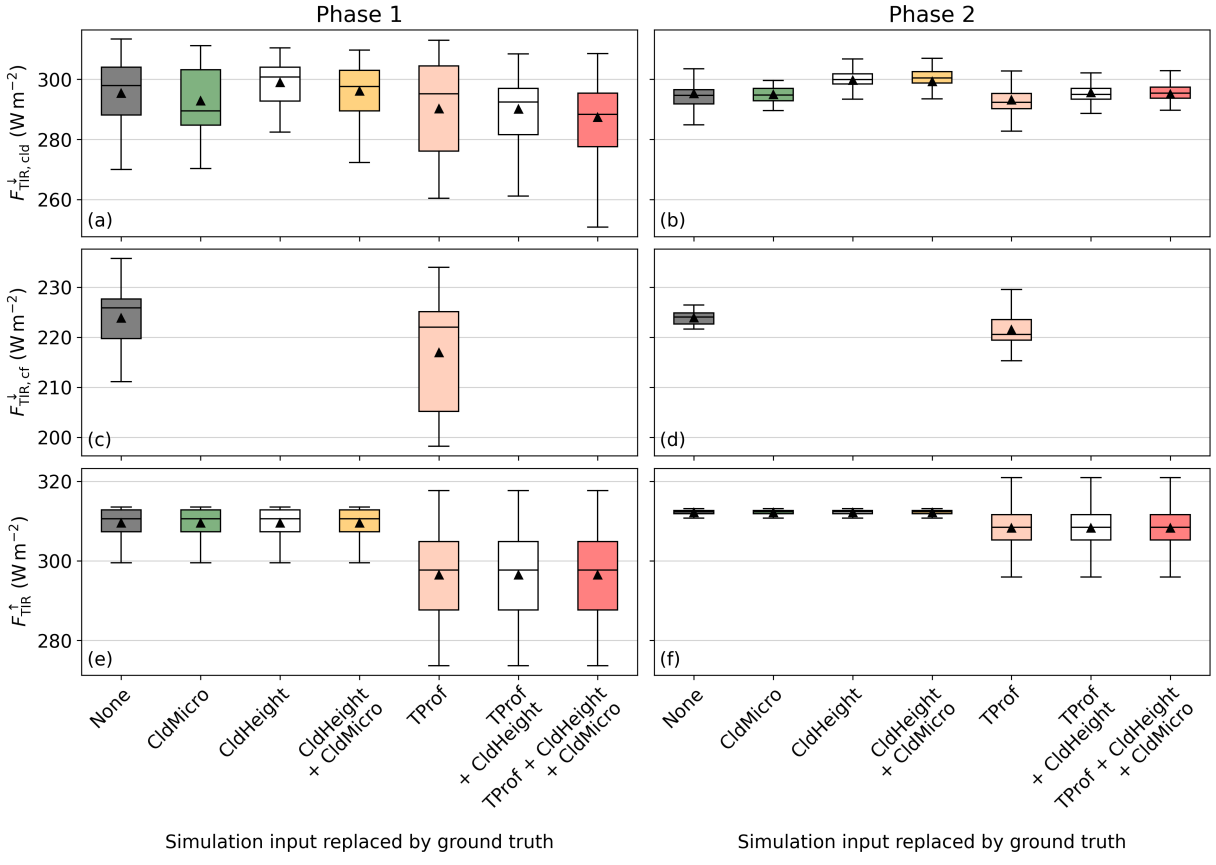

Figure 9. Statistics of (a,b) $F^{\downarrow}_{\mathrm{TIR}}$ in cloudy conditions, (c,d) $F^{\downarrow}_{\mathrm{TIR}}$ in cloud-free conditions, and (e,f) $F^{\uparrow}_{\mathrm{TIR}}$, simulated for various combinations of aircraft-measured and satellite-derived input and separated for (a,c,e) the first and (b,d,f) the second phase of ARCSIX. All boxplots are labeled according to the input parameters that are taken from the aircraft measurements ("ground truth"). The boxes indicate the IQR and the whiskers cover all data points that are max. $1.5 \times \mathrm{IQR}$ apart from the box; median and mean are represented by the horizontal line within the box and the triangle, respectively. Note that the statistics for combinations with missing boxplots in (c,d) do not differ from the closest distribution to the left.

https://doi.org/10.5194/egusphere-2026-2210
Preprint. Discussion started: 8 May 2026

aircraft observations, the effect of TProf is largely unaffected by atmospheric modification below the cloud and, thus, results in a larger $F_{\mathrm{TIR}}^{\downarrow}$ change for an identical CBT difference (Fig. 8). At the satellite-derived CBH, the mean temperature difference between GEOS-FP and dropsonde is small, but the larger temperature variability in the dropsonde profiles broadens the IQR of $F_{\mathrm{TIR}}^{\downarrow}$ (compare "TProf" vs. "None").

The results of cloudy $F_{\mathrm{TIR}}^{\downarrow}$ obtained for the second phase of ARCSIX are shown in Fig. 9b and exhibit a magnitude comparable to the first phase. In contrast, the weaker temperature variability (Fig. 5) causes generally narrower distributions. Pure satellite input yields a median of 295 $\mathrm{W\,m^{-2}}$ and an IQR of 292–297 $\mathrm{W\,m^{-2}}$. For the ground truth, a comparable median value is obtained. Compared to the first phase, this improved agreement is mainly related to two disparities. First, the aircraft-measured CldMicro alters the simulated $F_{\mathrm{TIR}}^{\downarrow}$ only marginally due to the predominance of optically thick clouds suggested by both satellite and aircraft observations (Fig. 7). Second, the counteracting effects of CldHeight and TProf compensate almost perfectly and modify the median of $F_{\mathrm{TIR}}^{\downarrow}$ by about 5 $\mathrm{W\,m^{-2}}$ each. The weaker effect of TProf compared to the first phase is consistent with the better agreement of the thermodynamic profiles and, consequently, the CBT between GEOS-FP and dropsondes (Figs. 5c, 8b).

In cloud-free conditions, represented by Figs. 9c and 9d, $F_{\mathrm{TIR}}^{\downarrow}$ depends on the thermodynamic profile only. During both campaign phases, simulations set up with GEOS-FP yield higher values compared to using the dropsonde profiles, which is related to the warmer low-level temperatures in GEOS-FP. During the first phase, the respective median values are 226 $\mathrm{W\,m^{-2}}$ and 222 $\mathrm{W\,m^{-2}}$, while slightly lower values of 224 $\mathrm{W\,m^{-2}}$ and 221 $\mathrm{W\,m^{-2}}$ are obtained for the second phase. Similar to cloudy conditions, the variability is lower during the second than during the first campaign phase, while the generally larger temperature variability in the dropsonde profiles compared to GEOS-FP widens the IQR for both phases.

Since the temperature profile is assumed to not change between cloudy and cloud-free conditions, $F_{\mathrm{TIR}}^{\uparrow}$ is identical in both situations and illustrated in Figs. 9e and 9f. Similar to $F_{\mathrm{TIR}}^{\downarrow}$ in cloud-free conditions, $F_{\mathrm{TIR}}^{\uparrow}$ depends solely on the input used for TProf, as it is driven by the surface skin temperature only. GEOS-FP systematically overestimates the surface temperature measured by the KT-19 (Fig. 5). This overestimation of on average 3 K during the first and 1 K during the second phase decreases the median $F_{\mathrm{TIR}}^{\uparrow}$ from 311 $\mathrm{W\,m^{-2}}$ to 298 $\mathrm{W\,m^{-2}}$ and from 312 $\mathrm{W\,m^{-2}}$ to 308 $\mathrm{W\,m^{-2}}$, respectively, when the GEOS-FP profile is replaced by the dropsonde (KT-19) observations. These numbers reflect the warming of the surface over the summer months, which is poorly represented by GEOS-FP. Again, the stronger variability in measured surface temperature and a generally weaker surface temperature variability during the second phase of ARCSIX are imprinted in the widths of the IQR.

4.2 Solar irradiances

The main drivers of the solar CRE are the microphysical cloud properties, the surface albedo, and the SZA. As the SZA calculated for a given time and location is invariable between aircraft- and satellite-derived simulation input, only the effects of aircraft–satellite differences of the former two drivers on the net solar irradiance $F_{\mathrm{sol}}^{\mathrm{net}}$ are analyzed.

https://doi.org/10.5194/egusphere-2026-2210
Preprint. Discussion started: 8 May 2026

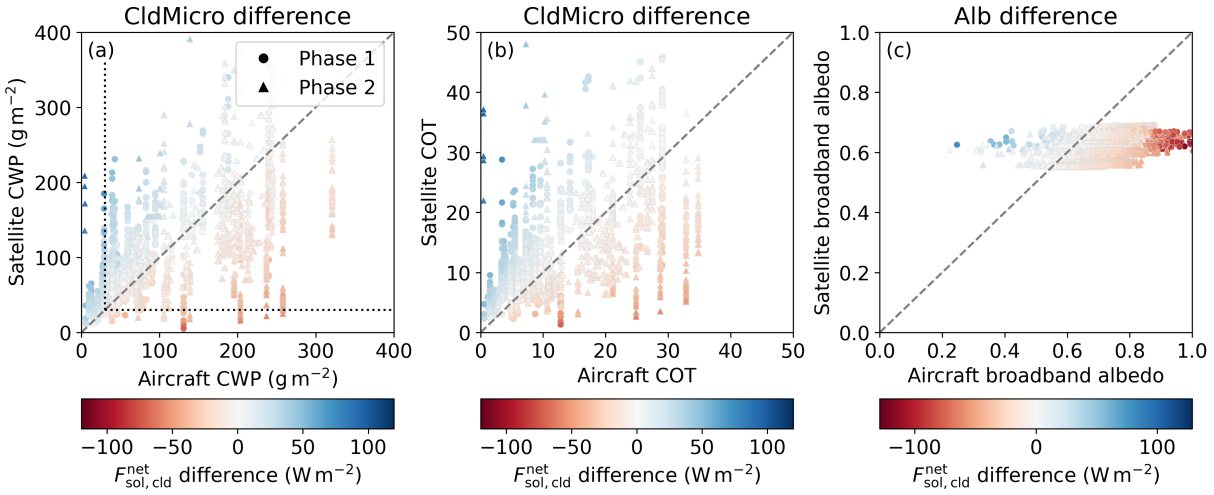

Figure 10. Aircraft- versus satellite-derived (a) CWP and (b) COT, separated for the first (dots) and second (triangles) phase of ARCSIX. The color-codings indicate the differences between F^{net}_{sol} in cloudy conditions resulting from simulations with satellite- and aircraft-derived input for CldMicro (aircraft minus satellite), while the remaining input parameters are taken from satellite observations. The black dotted lines in (a) mark the threshold of 30 g m^{-2} used to separate optically thin and thick clouds. (c) Same as (a) and (b), but for aircraft-derived versus cloud-retrieval broadband albedo, where the color-coding indicates the differences in F^{net}_{sol} resulting from the distinct input for Alb.

4.2.1 Impact of microphysical cloud properties

Similar to Fig. 7, aircraft- against satellite-derived CWP and the difference in simulated F^{net}_{sol} corresponding to the discrepancy between the two (aircraft minus satellite input) are shown in Fig. 10a for each data point. The simulation input for CldHeight, TProf, and Alb is completely based on satellite data. The sensitivity of F^{net}_{sol} to the CWP shows a fairly distinct characteristic compared to the TIR spectral range, as F^{net}_{sol} is still sensitive to CWPs larger than 30 g m^{-2}. Nevertheless, the fading colors for larger CWP values suggest that the sensitivity slightly decreases with increasing CWP. The dashed line, along which aircraft- and satellite-derived CWP are equal, does not well separate positive and negative differences in F^{net}_{sol}. This inconsistency is probably related to the slight overestimation of the combined ice–liquid CER by the satellite observations, which causes a positive bias of the satellite-derived F^{net}_{sol} (negative difference) for identical CWP values. As indicated by Fig. 10b, the COT, combining the effects of CWP and CER, correlates better with F^{net}_{sol} and irradiance differences of 0 are well distributed along the 1:1-line of aircraft- and satellite-derived COT. Although positive and negative F^{net}_{sol} differences are revealed for both phases of ARCSIX, the distribution of the markers and the corresponding colors imply that the statistical overestimation and underestimation of the COT by the satellite observations mainly causes a smaller and larger F^{net}_{sol} during the first and second phase of ARCSIX, respectively.

https://doi.org/10.5194/egusphere-2026-2210
Preprint. Discussion started: 8 May 2026

4.2.2 Impact of surface albedo

Figure 10c shows the $F_{\mathrm{sol}}^{\mathrm{net}}$ difference resulting from the contrast in surface albedo between the data derived from aircraft observations and used for the satellite cloud retrievals. The simulations used for this comparison rely on the satellite products and GEOS-FP for input of cloud and thermodynamic properties. The low bias in cloud-retrieval broadband surface albedo during both campaign phases indicated by Fig. 6 is also obvious in Fig. 10c for most data points and leads to an underestimation of the corresponding $F_{\mathrm{sol}}^{\mathrm{net}}$ (negative differences). Due to the lower SZA, this underestimation is stronger during the first campaign phase for a given albedo discrepancy.

4.2.3 Statistical simulation results

In analogy to the TIR irradiances, Fig. 11 presents box-whisker statistics of simulated solar irradiance components for different combinations of satellite- and aircraft-derived input parameters. As some drivers affect only one of the spectral regions, these combinations partly differ from those shown for the TIR counterparts.

For the first phase of ARCSIX, Fig. 11a displays the results of $F_{\mathrm{sol}}^{\mathrm{net}}$ under cloudy conditions. Pure satellite-derived simulation input (labeled "None") yields a median of 105 $\mathrm{W\,m^{-2}}$ and an IQR of 84–119 $\mathrm{W\,m^{-2}}$. Compared to the TIR range, the wider IQR indicates a stronger sensitivity of the solar irradiances to environmental variability, whereas differences in IQR width among the configurations shown in Fig. 11 are relatively small. The ground truth exhibits a substantially lower median of 64 $\mathrm{W\,m^{-2}}$. This decline in $F_{\mathrm{sol}}^{\mathrm{net}}$ is dominated by the surface albedo discrepancy, while a change in CldMicro has a counteracting effect (Fig. 10). Replacing only CldMicro with aircraft-measured properties ("CldMicro") decreases the COT and increases the median $F_{\mathrm{sol}}^{\mathrm{net}}$ by 9 $\mathrm{W\,m^{-2}}$. In contrast, the decrease induced by the higher aircraft-measured albedo alone amounts to 47 $\mathrm{W\,m^{-2}}$ ("Alb"). Aircraft–satellite differences in CldHeight and TProf have negligible effects on the solar irradiances, with deviations below 1 $\mathrm{W\,m^{-2}}$ across all components shown in Fig. 11.

The differences in $F_{\mathrm{sol}}^{\mathrm{net}}$ arise from the individual effects of CldMicro and Alb on $F_{\mathrm{sol}}^{\downarrow}$ and $F_{\mathrm{sol}}^{\uparrow}$, which partly compensate and are shown in Figs. 11b and 11c, respectively. The effect of CldMicro primarily affects $F_{\mathrm{sol}}^{\downarrow}$, increasing its median by 13 $\mathrm{W\,m^{-2}}$ following a replacement of satellite-derived simulation input by aircraft measurements ("None" vs. "CldMicro"). This increase is only weakly propagated to $F_{\mathrm{sol}}^{\uparrow}$ through surface reflection (2 $\mathrm{W\,m^{-2}}$). The analogous effect of Alb is stronger for $F_{\mathrm{sol}}^{\uparrow}$ than for $F_{\mathrm{sol}}^{\downarrow}$, increasing the medians by 81 $\mathrm{W\,m^{-2}}$ and 45 $\mathrm{W\,m^{-2}}$, respectively ("Alb" vs. "None"). The albedo effect on $F_{\mathrm{sol}}^{\downarrow}$ is mainly related to enhanced multiple reflections between cloud and surface due to the higher aircraft-measured surface albedo and, interestingly, more impactful than the difference in COT between satellite and aircraft observations.

Under cloud-free conditions, which are represented by Fig. 11d, $F_{\mathrm{sol}}^{\mathrm{net}}$ depends on the ineffective thermodynamic profile and the surface albedo only. Similar to cloudy conditions, replacing the cloud-retrieval surface albedo with the SSFR measurements reduces the median from 199 $\mathrm{W\,m^{-2}}$ to 116 $\mathrm{W\,m^{-2}}$. Because of the generally higher solar irradiances in cloud-free conditions, this decrease is more pronounced than in cloudy conditions.

Figures 11e–h reveal that, during the second phase of ARCSIX, the on average higher SZA compared to the first phase (70° vs. 62°) causes generally lower solar irradiances. For cloudy conditions (Fig. 11e), the purely satellite-based simulations result

https://doi.org/10.5194/egusphere-2026-2210
Preprint. Discussion started: 8 May 2026

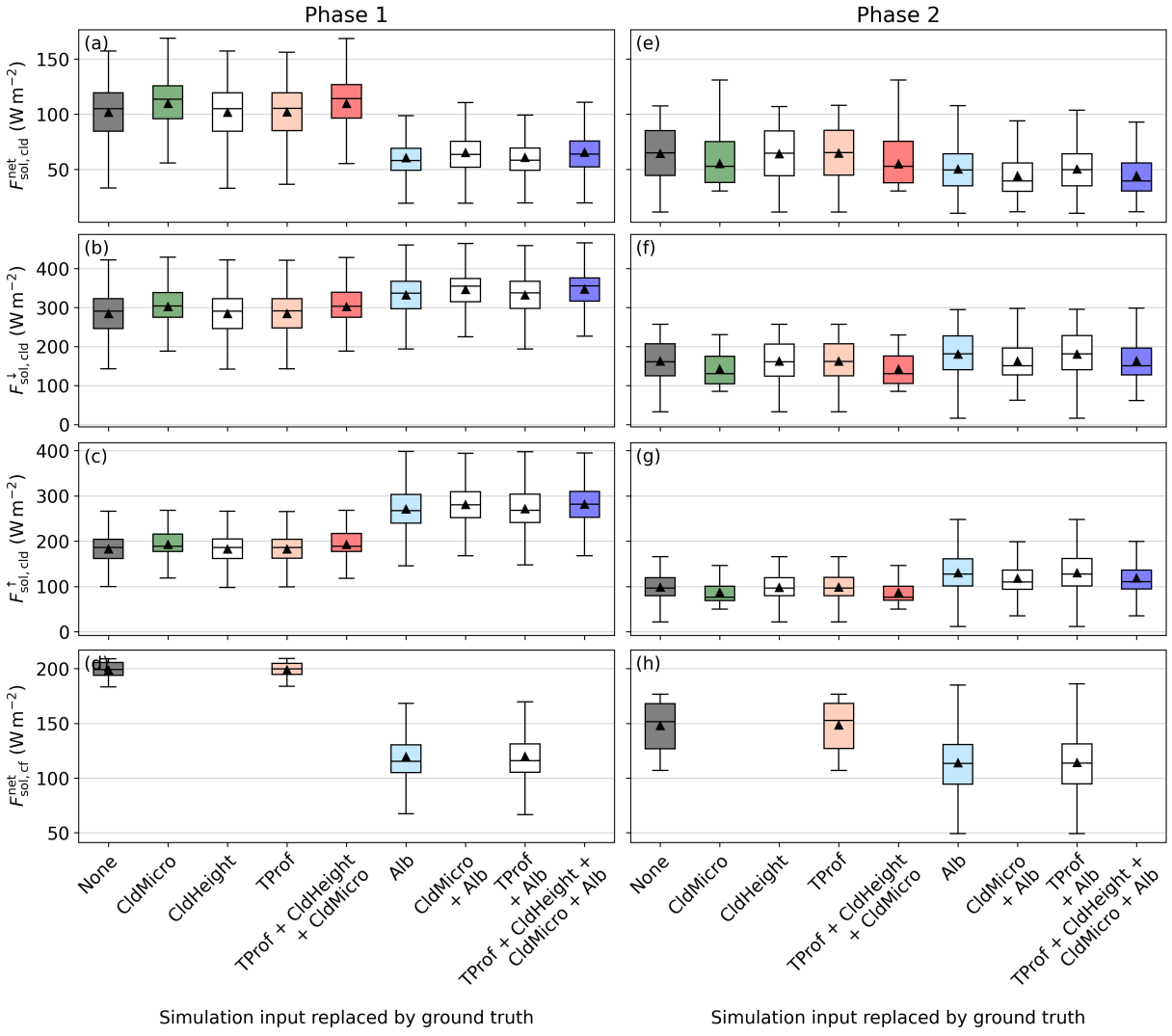

Figure 11. Same as Fig. 9, but for of (a,e) $F^{\mathrm{net}}_{\mathrm{sol}}$ in cloudy conditions, (b,f) $F^{\downarrow}_{\mathrm{sol}}$ in cloudy conditions, (c,g) $F^{\uparrow}_{\mathrm{sol}}$ in cloudy conditions, and (d,h) $F^{\mathrm{net}}_{\mathrm{sol}}$ in cloud-free conditions, separated for (a–d) the first and (e–h) the second phase of ARCSIX.

https://doi.org/10.5194/egusphere-2026-2210
Preprint. Discussion started: 8 May 2026

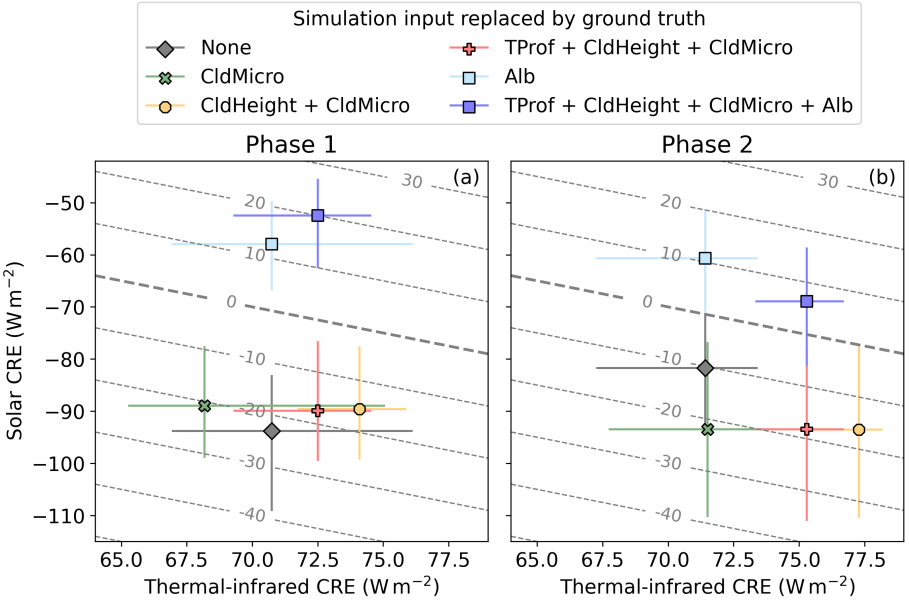

Figure 12. Statistics of simulated TIR and solar CRE for selected combinations of aircraft-measured and satellite-derived input (see legend), separated for (a) the first and (b) the second phase of ARCSIX. The colors corresponding to the different combinations are identical to Figs. 9 and 11 and the symbols and lines represent the median and IQR, respectively. The background contours indicate isolines of the total CRE in $\mathrm{W\,m^{-2}}$.

in a median $F_{\mathrm{sol}}^{\mathrm{net}}$ of $65\,\mathrm{W\,m^{-2}}$ ("None"), compared to $40\,\mathrm{W\,m^{-2}}$ for the ground truth. Again, the effect of Alb dominates over the effect of CldMicro. However, in contrast to the first phase, the isolated changes of CldMicro and Alb both reduce the median of $F_{\mathrm{sol}}^{\mathrm{net}}$ by $12\,\mathrm{W\,m^{-2}}$ and $15\,\mathrm{W\,m^{-2}}$, respectively. Apart from the sign change in the effect of CldMicro, the conclusions for $F_{\mathrm{sol}}^{\downarrow}$ and $F_{\mathrm{sol}}^{\uparrow}$ (Figs. 11f and 11g) do not depart from those drawn for the first phase of ARCSIX. The effect of CldMicro is larger for $F_{\mathrm{sol}}^{\downarrow}$ ($31\,\mathrm{W\,m^{-2}}$) than for $F_{\mathrm{sol}}^{\uparrow}$ ($20\,\mathrm{W\,m^{-2}}$), while the effect of Alb is dominated by $F_{\mathrm{sol}}^{\uparrow}$ ($31\,\mathrm{W\,m^{-2}}$ vs. $20\,\mathrm{W\,m^{-2}}$). Although both effects amplify for $F_{\mathrm{sol}}^{\mathrm{net}}$, they partially compensate for the individual irradiance components. The characteristics of the cloud-free $F_{\mathrm{sol}}^{\mathrm{net}}$ (Fig. 11h) closely resemble those of the first campaign phase. Simulations using the low-biased cloud-retrieval surface albedo yield a median of $152\,\mathrm{W\,m^{-2}}$, which is significantly larger compared to $114\,\mathrm{W\,m^{-2}}$ resulting from the SSRF measurements. A notable feature is the wider IQR, which likely reflects the stronger albedo variability compared to the first phase.

4.3 Total cloud radiative effect

For selected combinations of satellite- and aircraft-derived simulation input, Fig. 12 displays the statistics of TIR and solar CRE against each other. This illustration allows to directly assess the total warming or cooling effect of clouds during ARCSIX. The data of the first campaign phase are represented by Fig. 12a. Initializing the simulations with satellite data alone yields a median TIR CRE of about $71\,\mathrm{W\,m^{-2}}$ and a median solar CRE of $-94\,\mathrm{W\,m^{-2}}$, which combine to a total cooling effect

https://doi.org/10.5194/egusphere-2026-2210
Preprint. Discussion started: 8 May 2026

of the clouds. This cooling effect is only slightly reduced when the simulation input for CldMicro is replaced with in situ measurements, because the 3 $\mathrm{W\,m^{-2}}$ weakening of $F_{\mathrm{TIR}}^{\downarrow}$ (Fig. 9a) is compensated by a 5 $\mathrm{W\,m^{-2}}$ strengthening of $F_{\mathrm{sol}}^{\mathrm{net}}$ (Fig. 11a) under cloudy conditions. Similar to CldMicro, replacing the input for CldHeight with aircraft-derived values exclusively affects the irradiances in cloudy conditions. As a result of this input replacement, the TIR (and total) CRE increases by an additional 6 $\mathrm{W\,m^{-2}}$, consistent with the lower and, therefore, warmer cloud bases. Changing TProf from GEOS-FP to dropsonde input counteracts the effect of CldHeight on the TIR CRE. However, in contrast to the cloudy $F_{\mathrm{TIR}}^{\downarrow}$, where both effects compensate almost completely (Fig. 9a), the decrease in TIR CRE due to the modified TProf is only 2 $\mathrm{W\,m^{-2}}$, since the underlying differences in $F_{\mathrm{TIR}}^{\downarrow}$ partly compensate for cloudy and cloud-free conditions. As discussed earlier, the influence of both CldHeight and TProf is small in the solar range, altering the solar CRE by less than 1 $\mathrm{W\,m^{-2}}$. Among the configurations discussed so far, the median total CRE revealed only a weak variability and ranged between $-23\,\mathrm{W\,m^{-2}}$ and $-16\,\mathrm{W\,m^{-2}}$. However, the use of the measured surface albedo in the simulations leads to a cloud warming effect of approximately 20 $\mathrm{W\,m^{-2}}$. This switch of the sign of the total CRE corresponds to an increase in the solar CRE (i. e., weakening cooling effect) by roughly 35 $\mathrm{W\,m^{-2}}$, which is related to the stronger reduction in $F_{\mathrm{sol}}^{\mathrm{net}}$ for cloud-free than for cloudy conditions (Figs. 11c and 11d).

As indicated by Fig. 12b, the second phase of ARCSIX exhibits a broadly similar pattern. The main differences compared to the first phase arise from the larger SZA and differences in CldMicro. While the median of the purely satellite-derived TIR CRE is nearly identical to the first phase (71 $\mathrm{W\,m^{-2}}$), the SZA difference causes an absolutely lower median solar CRE of $-82\,\mathrm{W\,m^{-2}}$. Consequently, the total cooling effect suggested by the satellite input is weaker during the second phase despite a similar satellite-derived COT. Replacing CldMicro with the aircraft-measured cloud properties largely compensates for this weakening because of the significantly thicker clouds prevailing during the second phase. The resulting median of the solar CRE is $-93\,\mathrm{W\,m^{-2}}$. The TIR CRE for replaced CldMicro remains nearly unchanged due to the predominantly opaque clouds and is, therefore, about 3 $\mathrm{W\,m^{-2}}$ higher than during the first phase. Accordingly, the medians obtained when additionally replacing the input for CldHeight and CldHeight+TProf with aircraft measurements are shifted towards larger values. As for the first phase, the most pronounced change in the solar and total CRE results from the surface albedo difference between assumptions for the satellite cloud retrievals and SSFR observations. Although the second phase shows a slightly smaller reduction in the solar cooling effect (about 25 $\mathrm{W\,m^{-2}}$), which is caused by both the lower SZA and smaller albedo discrepancies, the median total CRE still transforms into a warming effect of around 5 $\mathrm{W\,m^{-2}}$. In contrast to the first phase, however, the associated interquartile range suggests that this transformation does not occur for all data points. Furthermore, the opposing effects of CldMicro and Alb in the solar range lead to a smaller bias of the satellite-derived total CRE relative to the ground truth than during the first phase of ARCSIX.

The previous analyses demonstrate that satellite-derived CRE estimates can be strongly biased by deficiencies of satellite retrievals and ancillary data in the Arctic. In particular, the simulated CRE suffers from the poorly represented and negatively biased surface albedo assumed for the satellite retrievals, which can cause a cooling effect although clouds actually warm the surface. In contrast, uncertainties in other satellite-derived properties are less critical and typically lead to CRE deviations of only a few $\mathrm{W\,m^{-2}}$. Despite individual drivers revealing significant biases (e. g., CBH), their effects often compensate partially.

https://doi.org/10.5194/egusphere-2026-2210
Preprint. Discussion started: 8 May 2026

Together with the generally weaker sensitivity to these parameters, this compensation limits the resulting inaccuracies of the CRE in the TIR range.

5 Conclusions

The performance of MODIS and VIIRS cloud products, a statistical surface albedo product scaled to account for sea ice melt, and thermodynamic profiles by the GEOS-FP analysis over Arctic sea ice were evaluated against aircraft measurements in this paper. These aircraft measurements were provided by in situ cloud probes, spectroradiometers, and dropsondes during ARCSIX between May and August 2024. Furthermore, the discrepancies in SRB and CRE resulting from radiative transfer simulations initialized with the satellite and aircraft observations were investigated and the effects of individual drivers were assessed by successively replacing satellite-derived simulation input with the aircraft-measured data. The point-wise collocated aircraft- and satellite-derived input parameters and simulated SRB and CRE were aggregated for multiple cases and analyzed statistically for the two campaign phases.

During the first phase of ARCSIX, the COT derived from the satellite data overestimated the aircraft measurements, while an underestimation was observed during the second phase. However, only for the first campaign phase affected this bias the TIR SRB and CRE, which shifted to on average 2.5 $\mathrm{W\,m^{-2}}$ larger values for the satellite-derived cloud properties, whereas the dominance of optically thick, opaque clouds prevented the TIR irradiances from a serious shift during the second phase. The mean satellite-derived solar CRE was roughly 8 $\mathrm{W\,m^{-2}}$ lower (stronger cooling effect) and 9 $\mathrm{W\,m^{-2}}$ higher for the first and second phase, respectively. The combined discrepancy between satellite- and aircraft-derived total CRE is rather weak despite the lack of a general correlation between aircraft- and satellite-derived COT that probably results from measurement uncertainties and different spatial resolutions. In contrast to the results reported by Chen et al. (2021), clouds undetected by the MODIS and VIIRS retrievals were rarely encountered in the cases analyzed here, mainly because the flight plans were based on clouds clearly visible in satellite images. Nevertheless, the cloud detection problem should not be ignored as a potential source of uncertainty for satellite-based SRB estimates and addressed in upcoming research.

The cloud height obtained from the satellite retrievals showed a significant overestimation on the order of 1 km, which is more severe for the VIIRS (on average 1730 m) than for the MODIS (725 m) retrieval algorithm. During both phases of ARCSIX, these higher satellite-derived clouds resulted in 1–3 K colder CBTs and reduced the TIR SRB and CRE by about 3–4 $\mathrm{W\,m^{-2}}$ on average. However, this reduction was partly compensated by effects of discrepant air temperature profiles between dropsondes and GEOS-FP. Especially during the first campaign phase, the air temperature in the lowest 500 m was too high and led to an underestimated strength of the capping inversion in GEOS-FP. Likely, the uncertainties in satellite-retrieved cloud height are largely linked to a similar bias in the ancillary temperature profiles, which require a sufficient accuracy to precisely assign an altitude to the measured brightness temperatures. Therefore, testing the performance of cloud height retrievals for real measured temperature profiles in future work will be beneficial to disentangle the impact of retrieval algorithm and temperature input on the cloud height uncertainty. The solar radiation is weakly affected by both cloud height and thermodynamic profile differences.

https://doi.org/10.5194/egusphere-2026-2210
Preprint. Discussion started: 8 May 2026

The spectral sea ice albedo assumed for the satellite-based cloud retrievals was consistently too low compared to the aircraft measurements. This underestimation is primarily related to the overestimated sea ice melt during summer, which caused a larger disagreement for the first than for the second phase of ARCSIX. As a result, the corresponding solar SRB showed a significant high bias, which is stronger in cloud-free than in cloudy conditions and results in a lower CRE (stronger solar cooling effect) than actually present.

In total, the dominance of optically thick clouds, compensating effects between cloud height and thermodynamic profile, and a generally weaker sensitivity limit the variability in TIR CRE resulting from the different combinations of aircraft- and satellite-derived simulation input. The median values ranged between $68\,\mathrm{W\,m^{-2}}$ and $74\,\mathrm{W\,m^{-2}}$ for the first and between $71\,\mathrm{W\,m^{-2}}$ and $77\,\mathrm{W\,m^{-2}}$ for the second phase of ARCSIX. In contrast, the solar cooling effect strongly varied between $-90\,\mathrm{W\,m^{-2}}$ for the cloud-retrieval and $-55\,\mathrm{W\,m^{-2}}$ (first phase) or $-65\,\mathrm{W\,m^{-2}}$ (second phase) for the aircraft-measured surface albedo. For both campaign phases, this surface albedo discrepancy caused a cooling effect of clouds using the albedo assumed for the satellite cloud retrievals, although a warming effect was present in reality.

The findings of this study imply that the albedo assumed for the MODIS and VIIRS cloud retrievals do not well represent Arctic sea ice conditions during the analyzed period, causing a bias in the simulated CRE, but also limiting the accuracy of satellite-derived cloud microphysical properties. A too low surface albedo is expected to yield an overestimated COT, although the observations of this study support this suspicion only partly. Nevertheless, as a low bias in sea ice albedo is a general problem in climate models and remote sensing applications (Huang et al., 2022; Kim and Taylor, 2026), a more realistic representation of the surface albedo and associated processes, such as sea ice melt or melt pond formation, is required for more accurate cloud retrievals and radiation budget calculations in the Arctic. The results presented here serve as a first step towards this improvement using ARCSIX field campaign observations. Simultaneously, current research focuses on improving the kernel-based satellite retrieval of spectral albedo over snow and sea ice surfaces by means of airborne measurements of spectral surface albedo and directional surface reflectance performed during ARCSIX.

Data availability. The aircraft data analyzed in this study are published at the NASA Langley Atmospheric Science Data Center. In situ cloud data from P-3 and Learjet are available at NASA/LARC/SD/ASDC (2025b, https://doi.org/10.5067/SUBORBITAL/ARCSIX/DATA001/P3B/Cloud_AircraftInSitu_1) and NASA/LARC/SD/ASDC (2025a, https://doi.org/10.5067/SUBORBITAL/ARCSIX/DATA001/Learjet/Cloud_AircraftInSitu_1), respectively. The SSFR observations are obtained from NASA/LARC/SD/ASDC (2025e, https://doi.org/10.5067/SUBORBITAL/ARCSIX/DATA001/P3B/Radiation_AircraftInSitu_1) and the dropsonde profiles can be found at NASA/LARC/SD/ASDC (2025c, https://doi.org/10.5067/SUBORBITAL/ARCSIX/DATA001/G3/Dropsondes_1). NASA/LARC/SD/ASDC (2025d, https://doi.org/10.5067/SUBORBITAL/ARCSIX/DATA001/P3B/MetNav_AircraftInSitu_1) contains the position and meteorological data from the P-3, including the KT-19 measurements. Satellite cloud products from MODIS observations aboard Terra (MODIS Atmosphere Science Team, 2017a) and Aqua (MODIS Atmosphere Science Team, 2017b), and VIIRS observations aboard Suomi-NPP (VIIRS Atmosphere Science Team SSEC University Of Wisconsin-Madison, 2019) and NOOA-20 (VIIRS Atmosphere Science Team SSEC University Of Wisconsin-Madison, 2021) were used.

https://doi.org/10.5194/egusphere-2026-2210
Preprint. Discussion started: 8 May 2026

Author contributions. SB performed the analysis, drafted the manuscript, and developed the methodology of the study together with KSS. KSS and MW helped with the interpretation of the results. HC and YWC processed the SSFR albedo data. KGM and CAP provided the satellite-based albedo product. All authors contributed to reviewing and editing the manuscript.

Competing interests. The authors declare that there are no conflicts of interest.

Acknowledgements. The aircraft data used within this study were obtained from the NASA Langley Research Center Atmospheric Science Data Center. The GEOS data have been provided by the Global Modeling and Assimilation Office (GMAO) at NASA Goddard Space Flight Center. We gratefully acknowledge the funding by the Deutsche Forschungsgemeinschaft (DFG, German Research Foundation) – Projektnummer 268020496 – TRR 172, within the Transregional Collaborative Research Center "ArctiC Amplification: Climate Relevant Atmospheric and SurfaCe Processes, and Feedback Mechanisms (AC)^3.

https://doi.org/10.5194/egusphere-2026-2210
Preprint. Discussion started: 8 May 2026

References

Baker, B. and Lawson, R. P.: Improvement in Determination of Ice Water Content from Two-Dimensional Particle Imagery. Part I: Image-to-Mass Relationships, J. Appl. Meteorol. Climatol., 45, 1282–1290, https://doi.org/10.1175/jam2398.1, 2006.

Baum, B. A., Menzel, W. P., Frey, R. A., Tobin, D. C., Holz, R. E., Ackerman, S. A., Heidinger, A. K., and Yang, P.: MODIS Cloud-Top Property Refinements for Collection 6, J. Appl. Meteorol. Climatol., 51, 1145–1163, https://doi.org/10.1175/jamc-d-11-0203.1, 2012.

Becker, S., Ehrlich, A., Schäfer, M., and Wendisch, M.: Airborne observations of the surface cloud radiative effect during different seasons over sea ice and open ocean in the Fram Strait, Atmos. Chem. Phys., 23, 7015–7031, https://doi.org/10.5194/acp-23-7015-2023, 2023.

Becker, S., Ehrlich, A., Schäfer, M., and Wendisch, M.: Quantifying the impact of solar zenith angle, cloud optical thickness, and surface albedo on the solar radiative effect of Arctic low-level clouds over open ocean and sea ice, Atmos. Chem. Phys., 25, 12 831–12 842, https://doi.org/10.5194/acp-25-12831-2025, 2025.

Bennartz, R., Shupe, M. D., Turner, D. D., Walden, V. P., Steffen, K., Cox, C. J., Kulie, M. S., Miller, N. B., and Pettersen, C.: July 2012 Greenland melt extent enhanced by low-level liquid clouds, Nature, 496, 83–86, https://doi.org/10.1038/nature12002, 2013.

Buras, R., Dowling, T., and Emde, C.: New secondary-scattering correction in DISORT with increased efficiency for forward scattering, J. Quant Spectrosc. Radiat. Transf., 112, 2028–2034, https://doi.org/10.1016/j.jqsrt.2011.03.019, 2011.

Cesana, G., Kay, J. E., Chepfer, H., English, J. M., and de Boer, G.: Ubiquitous low-level liquid-containing Arctic clouds: New observations and climate model constraints from CALIPSO-GOCCP, Geophys. Res. Lett., 39, https://doi.org/10.1029/2012gl053385, 2012.

Chen, H., Schmidt, S., King, M. D., Wind, G., Bucholtz, A., Reid, E. A., Segal-Rozenhaimer, M., Smith, W. L., Taylor, P. C., Kato, S., and Pilewskie, P.: The effect of low-level thin arctic clouds on shortwave irradiance: evaluation of estimates from spaceborne passive imagery with aircraft observations, Atmos. Meas. Tech., 14, 2673–2697, https://doi.org/10.5194/amt-14-2673-2021, 2021.

Chylek, P., Folland, C., Klett, J. D., Wang, M., Hengartner, N., Lesins, G., and Dubey, M. K.: Annual Mean Arctic Amplification 1970–2020: Observed and Simulated by CMIP6 Climate Models, Geophys. Res. Lett., 49, https://doi.org/10.1029/2022gl099371, 2022.

Cohen, J., Zhang, X., Francis, J., Jung, T., Kwok, R., Overland, J., Ballinger, T. J., Bhatt, U. S., Chen, H. W., Coumou, D., Feldstein, S., Gu, H., Handorf, D., Henderson, G., Ionita, M., Kretschmer, M., Laliberte, F., Lee, S., Linderholm, H. W., Maslowski, W., Peings, Y., Pfeiffer, K., Rigor, I., Semmler, T., Stroeve, J., Taylor, P. C., Vavrus, S., Vihma, T., Wang, S., Wendisch, M., Wu, Y., and Yoon, J.: Divergent consensuses on Arctic amplification influence on midlatitude severe winter weather, Nat. Clim. Change, 10, 20–29, https://doi.org/10.1038/s41558-019-0662-y, 2020.

Crawford, A. D., Lukovich, J. V., McCrystall, M. R., Stroeve, J. C., and Barber, D. G.: Reduced Sea Ice Enhances Intensification of Winter Storms over the Arctic Ocean, J. Clim., 35, 3353–3370, https://doi.org/10.1175/jcli-d-21-0747.1, 2022.

Ebell, K., Nomokonova, T., Maturilli, M., and Ritter, C.: Radiative Effect of Clouds at Ny-Ålesund, Svalbard, as Inferred from Ground-Based Remote Sensing Observations, J. Appl. Meteorol. Clim., 59, 3–22, https://doi.org/10.1175/jamc-d-19-0080.1, 2020.

Emde, C., Buras-Schnell, R., Kylling, A., Mayer, B., Gasteiger, J., Hamann, U., Kylling, J., Richter, B., Pause, C., Dowling, T., and Bugliaro, L.: The libRadtran software package for radiative transfer calculations (version 2.0.1), Geosci. Model Dev., 9, 1647–1672, https://doi.org/10.5194/gmd-9-1647-2016, 2016.

Gasteiger, J., Emde, C., Mayer, B., Buras, R., Buehler, S., and Lemke, O.: Representative wavelengths absorption parameterization applied to satellite channels and spectral bands, J. Quant. Spectrosc. Radiat. Transfer, 148, 99–115, https://doi.org/10.1016/j.jqsrt.2014.06.024, 2014.

https://doi.org/10.5194/egusphere-2026-2210
Preprint. Discussion started: 8 May 2026

Goosse, H., Kay, J. E., Armour, K. C., Bodas-Salcedo, A., Chepfer, H., Docquier, D., Jonko, A., Kushner, P. J., Lecomte, O., Massonnet, F., Park, H.-S., Pithan, F., Svensson, G., and Vancoppenolle, M.: Quantifying climate feedbacks in polar regions, Nat. Commun., 9, https://doi.org/10.1038/s41467-018-04173-0, 2018.

Hall, A.: The Role of Surface Albedo Feedback in Climate, J. Clim., 17, 1550–1568, https://doi.org/10.1175/1520-0442(2004)017<1550:trosaf>2.0.co;2, 2004.

Heidinger, A. K. and Pavolonis, M. J.: Gazing at Cirrus Clouds for 25 Years through a Split Window. Part I: Methodology, J. Appl. Meteorol. Climatol., 48, 1100–1116, https://doi.org/10.1175/2008jamc1882.1, 2009.

Hess, M., Koepke, P., and Schult, I.: Optical Properties of Aerosols and Clouds: The Software Package OPAC, Bull. Am. Meteorol. Soc., 79, 831–844, https://doi.org/10.1175/1520-0477(1998)079<0831:opoaac>2.0.co;2, 1998.

Heuzé, C. and Jahn, A.: The first ice-free day in the Arctic Ocean could occur before 2030, Nat. Commun., 15, https://doi.org/10.1038/s41467-024-54508-3, 2024.

Huang, Y., Chou, G., Xie, Y., and Soulard, N.: Radiative Control of the Interannual Variability of Arctic Sea Ice, Geophys. Res. Lett., 46, 9899–9908, https://doi.org/10.1029/2019gl084204, 2019.

Huang, Y., Taylor, P. C., Rose, F. G., Rutan, D. A., Shupe, M. D., Webster, M. A., and Smith, M. M.: Toward a more realistic representation of surface albedo in NASA CERES-derived surface radiative fluxes, Elem. Sci. Anth., 10, https://doi.org/10.1525/elementa.2022.00013, 2022.

Hünerbein, A., Bley, S., Horn, S., Deneke, H., and Walther, A.: Cloud mask algorithm from the EarthCARE Multi-Spectral Imager: the M-CM products, Atmos. Meas. Tech., 16, 2821–2836, https://doi.org/10.5194/amt-16-2821-2023, 2023.

Jahn, A., Holland, M. M., and Kay, J. E.: Projections of an ice-free Arctic Ocean, Nat. Rev. Earth Environ., 5, 164–176, https://doi.org/10.1038/s43017-023-00515-9, 2024.

Jeffries, M. O., Overland, J. E., and Perovich, D. K.: The Arctic shifts to a new normal0, Phys. Today, 66, 35–40, https://doi.org/10.1063/pt.3.2147, 2013.

Kapsch, M.-L., Graversen, R. G., Tjernström, M., and Bintanja, R.: The Effect of Downwelling Longwave and Shortwave Radiation on Arctic Summer Sea Ice, J. Clim., 29, 1143–1159, https://doi.org/10.1175/jcli-d-15-0238.1, 2016.

Karlsson, K.-G., Stengel, M., Meirink, J. F., Riihelä, A., Trentmann, J., Akkermans, T., Stein, D., Devasthale, A., Eliasson, S., Johansson, E., Håkansson, N., Solodovnik, I., Benas, N., Clerbaux, N., Selbach, N., Schröder, M., and Hollmann, R.: CLARA-A3: The third edition of the AVHRR-based CM SAF climate data record on clouds, radiation and surface albedo covering the period 1979 to 2023, Earth Syst. Sci. Data, 15, 4901–4926, https://doi.org/10.5194/essd-15-4901-2023, 2023.

Kato, S., Ackerman, T. P., Mather, J. H., and Clothiaux, E. E.: The k-distribution method and correlated-k approximation for a shortwave radiative transfer model, J. Quant. Spectrosc. Radiat. Transfer, 62, 109–121, https://doi.org/10.1016/s0022-4073(98)00075-2, 1999.

Kim, D. and Taylor, P. C.: What Factors Explain the Current Arctic Albedo and Its Future Change?, J. Geophys. Res.: Atmos., 131, https://doi.org/10.1029/2025jd044070, 2026.

Lawson, P., Gurganus, C., Woods, S., and Bruintjes, R.: Aircraft Observations of Cumulus Microphysics Ranging from the Tropics to Midlatitudes: Implications for a “New” Secondary Ice Process, J. Appl. Meteorol. Climatol., 74, 2899–2920, https://doi.org/10.1175/jas-d-17-0033.1, 2017.

Liang, S., Cheng, J., Jia, K., Jiang, B., Liu, Q., Xiao, Z., Yao, Y., Yuan, W., Zhang, X., Zhao, X., and Zhou, J.: The Global Land Surface Satellite (GLASS) Product Suite, Bull. Am. Meteorol. Soc., 102, E323–E337, https://doi.org/10.1175/bams-d-18-0341.1, 2021.

https://doi.org/10.5194/egusphere-2026-2210
Preprint. Discussion started: 8 May 2026

Liu, Y., Wang, Z., Sun, Q., Erb, A. M., Li, Z., Schaaf, C. B., Zhang, X., Román, M. O., Scott, R. L., Zhang, Q., Novick, K. A., Syndonia Bret-Harte, M., Petroy, S., and SanClements, M.: Evaluation of the VIIRS BRDF, Albedo and NBAR products suite and an assessment of continuity with the long term MODIS record, Remote Sens. Environ., 201, 256–274, https://doi.org/10.1016/j.rse.2017.09.020, 2017.

Loeb, N., Su, W., Doelling, D., Wong, T., Minnis, P., Thomas, S., and Miller, W.: Earth's Top-of-Atmosphere Radiation Budget, p. 67–84, Elsevier, https://doi.org/10.1016/b978-0-12-409548-9.10367-7, 2018.

Lucht, W., Schaaf, C., and Strahler, A.: An algorithm for the retrieval of albedo from space using semiempirical BRDF models, IEEE Trans. Geosci. Remote Sens., 38, 977–998, https://doi.org/10.1109/36.841980, 2000.

Luo, N., Li, J., Xiao, C., Fu, Y. H., Li, X., Sun, C., He, B., and Ding, R.: Slowdown of wintertime Arctic amplification since 2012, The Innovation Geoscience, 3, 100 130, https://doi.org/10.59717/j.xinn-geo.2024.100130, 2025.

Meier, W. N., Petty, A., Hendricks, S., Bliss, A., Kaleschke, L., Divine, D., Farrell, S., Gerland, S., Perovich, D., Ricker, R., Tian-Kunze, X., and Webster, M.: Sea Ice, in: Arctic Report Card 2024, edited by Moon, T. A., Druckenmiller, M. L., and Thoman, R. L., p. 41–50, https://doi.org/10.25923/aksk-7p66, 2024.

Miller, N. B., Shupe, M. D., Cox, C. J., Walden, V. P., Turner, D. D., and Steffen, K.: Cloud Radiative Forcing at Summit, Greenland, J. Clim., 28, 6267–6280, https://doi.org/10.1175/jcli-d-15-0076.1, 2015.

Minnis, P., Sun-Mack, S., Chen, Y., Chang, F.-L., Yost, C. R., Smith, W. L., Heck, P. W., Arduini, R. F., Bedka, S. T., Yi, Y., Hong, G., Jin, Z., Painemal, D., Palikonda, R., Scarino, B. R., Spangenberg, D. A., Smith, R. A., Trepte, Q. Z., Yang, P., and Xie, Y.: CERES MODIS Cloud Product Retrievals for Edition 4—Part I: Algorithm Changes, IEEE Trans. Geosci. Remote Sens., 59, 2744–2780, https://doi.org/10.1109/tgrs.2020.3008866, 2021.

MODIS Atmosphere Science Team: MODIS/Terra Atmosphere L2 Cloud Product (MOD06_L2), NASA Level 1 and Atmosphere Archive and Distribution System Distributed Active Archive Center, https://doi.org/10.5067/MODIS/MOD06_L2.061, 2017a.

MODIS Atmosphere Science Team: MODIS/Aqua Atmosphere L2 Cloud Product (MOD06_L2), NASA Level 1 and Atmosphere Archive and Distribution System Distributed Active Archive Center, https://doi.org/10.5067/MODIS/MYD06_L2.061, 2017b.

Moody, E. G., King, M. D., Schaaf, C. B., Hall, D. K., and Platnick, S.: Northern Hemisphere five-year average (2000–2004) spectral albedos of surfaces in the presence of snow: Statistics computed from Terra MODIS land products, Remote Sens. Environ., 111, 337–345, https://doi.org/10.1016/j.rse.2007.03.026, 2007.

Nakajima, T. and King, M. D.: Determination of the Optical Thickness and Effective Particle Radius of Clouds from Reflected Solar Radiation Measurements. Part I: Theory, J. Atmos. Sci., 47, 1878–1893, https://doi.org/10.1175/1520-0469(1990)047<1878:dotota>2.0.co;2, 1990.

NASA/LARC/SD/ASDC: ARCSIX Learjet In-Situ Cloud Data [Data set], NASA Langley Atmospheric Science Data Center DAAC, https://doi.org/10.5067/SUBORBITAL/ARCSIX/DATA001/Learjet/Cloud_AircraftInSitu_1, 2025a.

NASA/LARC/SD/ASDC: ARCSIX P-3B In-Situ Cloud Data [Data set], NASA Langley Atmospheric Science Data Center DAAC, https://doi.org/10.5067/SUBORBITAL/ARCSIX/DATA001/P3B/Cloud_AircraftInSitu_1, 2025b.

NASA/LARC/SD/ASDC: ARCSIX LaRC G-III Dropsonde Data [Data set], NASA Langley Atmospheric Science Data Center DAAC, https://doi.org/10.5067/SUBORBITAL/ARCSIX/DATA001/G3/Dropsondes_1, 2025c.

NASA/LARC/SD/ASDC: ARCSIX P-3B In-Situ Meteorology and Navigation Data [Data set], NASA Langley Atmospheric Science Data Center DAAC, https://doi.org/10.5067/SUBORBITAL/ARCSIX/DATA001/P3B/MetNav_AircraftInSitu_1, 2025d.

NASA/LARC/SD/ASDC: ARCSIX P-3B In-Situ Radiation Data [Data set], NASA Langley Atmospheric Science Data Center DAAC, https://doi.org/10.5067/SUBORBITAL/ARCSIX/DATA001/P3B/Radiation_AircraftInSitu_1, 2025e.

https://doi.org/10.5194/egusphere-2026-2210
Preprint. Discussion started: 8 May 2026

Noh, Y.-J., Forsythe, J. M., Miller, S. D., Seaman, C. J., Li, Y., Heidinger, A. K., Lindsey, D. T., Rogers, M. A., and Partain, P. T.: Cloud-Base Height Estimation from VIIRS. Part II: A Statistical Algorithm Based on A-Train Satellite Data, J. Atmos. Oceanic Technol., 34, 585–598, https://doi.org/10.1175/jtech-d-16-0110.1, 2017.

Peng, J., Yu, Y., Yu, P., and Liang, S.: The VIIRS Sea-Ice Albedo Product Generation and Preliminary Validation, Remote Sens., 10, 1826, https://doi.org/10.3390/rs10111826, 2018.

Pithan, F. and Mauritsen, T.: Arctic amplification dominated by temperature feedbacks in contemporary climate models, Nat. Geosci., 7, 181–184, https://doi.org/10.1038/ngeo2071, 2014.

Platnick, S., Li, J. Y., King, M. D., Gerber, H., and Hobbs, P. V.: A solar reflectance method for retrieving the optical thickness and droplet size of liquid water clouds over snow and ice surfaces, J. Geophys. Res.: Atmos., 106, 15 185–15 199, https://doi.org/10.1029/2000jd900441, 2001.

Platnick, S., Meyer, K. G., King, M. D., Wind, G., Amarasinghe, N., Marchant, B., Arnold, G. T., Zhang, Z., Hubanks, P. A., Holz, R. E., Yang, P., Ridgway, W. L., and Riedi, J.: The MODIS Cloud Optical and Microphysical Products: Collection 6 Updates and Examples From Terra and Aqua, IEEE Trans. Geosci. Remote Sens., 55, 502–525, https://doi.org/10.1109/tgrs.2016.2610522, 2017.

Platnick, S., Meyer, K., Wind, G., Holz, R. E., Amarasinghe, N., Hubanks, P. A., Marchant, B., Dutcher, S., and Veglio, P.: The NASA MODIS-VIIRS Continuity Cloud Optical Properties Products, Remote Sens., 13, 2, https://doi.org/10.3390/rs13010002, 2020.

Qu, Y., Liang, S., Liu, Q., Li, X., Feng, Y., and Liu, S.: Estimating Arctic sea-ice shortwave albedo from MODIS data, Remote Sens. Environ., 186, 32–46, https://doi.org/10.1016/j.rse.2016.08.015, 2016.

Rantanen, M., Karpechko, A. Y., Lipponen, A., Nordling, K., Hyvärinen, O., Ruosteenoja, K., Vihma, T., and Laaksonen, A.: The Arctic has warmed nearly four times faster than the globe since 1979, Commun. Earth Environ., 3, https://doi.org/10.1038/s43247-022-00498-3, 2022.

Schmidt, S. and Pilewskie, P.: Airborne measurements of spectral shortwave radiation in cloud and aerosol remote sensing and energy budget studies, in: Light Scattering Reviews, Vol. 6: Light Scattering and Remote Sensing of Atmosphere and Surface, edited by Kokhanovsky, A. A., p. 239–288, Springer, Berlin, Heidelberg, Germany, https://doi.org/10.1007/978-3-642-15531-4_6, 2012.

Scott, R. C., Rose, F. G., Stackhouse, P. W., Loeb, N. G., Kato, S., Doelling, D. R., Rutan, D. A., Taylor, P. C., and Smith, W. L.: Clouds and the Earth's Radiant Energy System (CERES) Cloud Radiative Swath (CRS) Edition 4 Data Product, J. Atmos. Oceanic Technol., 39, 1781–1797, https://doi.org/10.1175/jtech-d-22-0021.1, 2022.

Screen, J. A. and Simmonds, I.: The central role of diminishing sea ice in recent Arctic temperature amplification, Nature, 464, 1334–1337, https://doi.org/10.1038/nature09051, 2010.

Serreze, M. C. and Barry, R. G.: Processes and impacts of Arctic amplification: A research synthesis, Global Planet. Change, 77, 85–96, https://doi.org/10.1016/j.gloplacha.2011.03.004, 2011.

Serreze, M. C. and Francis, J. A.: The Arctic Amplification Debate, Climatic Change, 76, 241–264, https://doi.org/10.1007/s10584-005-9017-y, 2006.

Shupe, M. D. and Intrieri, J. M.: Cloud Radiative Forcing of the Arctic Surface: The Influence of Cloud Properties, Surface Albedo, and Solar Zenith Angle, J. Clim., 17, 616–628, https://doi.org/10.1175/1520-0442(2004)017<0616:crfota>2.0.co;2, 2004.

Stapf, J., Ehrlich, A., Jäkel, E., Lüpkes, C., and Wendisch, M.: Reassessment of shortwave surface cloud radiative forcing in the Arctic: consideration of surface-albedo–cloud interactions, Atmos. Chem. and Phys., 20, 9895–9914, https://doi.org/10.5194/acp-20-9895-2020, 2020.

https://doi.org/10.5194/egusphere-2026-2210
Preprint. Discussion started: 8 May 2026

Su, W., Corbett, J., Eitzen, Z., and Liang, L.: Next-generation angular distribution models for top-of-atmosphere radiative flux calculation from CERES instruments: methodology, Atmos. Meas. Tech., 8, 611–632, https://doi.org/10.5194/amt-8-611-2015, 2015.

Taylor, P. C., Sorooshian, A., Ueyama, R., Schmidt, S., Abboud, I., Allison, Q., Barry, K., Becker, S., Bender, H. A., Bennett, J. R., Blair, J. B., Bohn, N., Boisvert, L., Brown, M. D., Bruintjes, R., Bucholtz, A., Buzanowicz, M., Cairns, B., Calì Quaglia, F., Chemyakin, E., Chen, B., Chen, G., Chen, H., Chen, Y.-W., Cheng, Z., China, S., Chirica, D., Choi, Y., Colarco, P., Collister, B., Crosbie, E., Cross, M. J., Daniels, J., DeMott, P., DiGangi, J. P., di Sarra, A. G., Diskin, G. S., Dolinar, E. K., Edwards, E.-L., Ephraim, S., Evangeliou, N., Foskinis, R., Gallo, F., Gao, L., Gómez-Amo, J. L., Gonzalez, D., Groot Zwaaftink, C., Gupta, P., Heckman, I., Hendrickson, M., Hilario, M. R. A., Hirata, K., Hofton, M., Holen, A. L., Im, U., Khan, A. L., Kahn, R. A., Korolev, A. V., Kreidenweis, S., Krumpen, T., Kurtz, N., Lait, L., Lamkin, B., Landy, J., Lata, N. N., Lawson, P., LeBlanc, S., Leavor, S., Li, J., Markus, T., Maring, H., Massling, A. H., Mavis, C., McGinnity, F., Meyer, K., Mojica, G., Moore, R. H., Morris, P., Muscari, G., Nataraja, V., Nehrir, A. R., Nenes, A., Nowottnick, E. P., Ottaviani, M., Parker, C., Patnaude, R., Perez, M., Perkins, R. J., Peterson, C., Petty, A., Phothisane, S., Polashenski, C., Pratt, K. A., Preisler, K. M., Prytherch, J., Rabine, D., Redemann, J., Ryoo, J.-M., Schlosser, J., Selimovic, V., Shook, M. A., Silverman, M., Skov, H., Smirnov, A., Soloff, C., Solomon, A., Stamnes, S., Takeishi, A., Thompson, D. R., Thornhill, K. L., Tilling, R., Tjernström, M., Tosco, M., Valdelomar, P. C., Van Gilst, D., Wang, J., Wang, Z., Wasilewski, A., Wendisch, M., Wilder, B., Winstead, E. L., Wu, A., Xian, P., Zamora, L. M., Zhang, J., Zhang, L., Zhang, L., Ziemba, L., and Zuidema, P.: The Arctic Radiation–Cloud–Aerosol–Surface Interaction Experiment (ARCSIX) airborne campaign dataset, submitted to Earth Syst. Sci. Data, 2026.

VIIRS Atmosphere Science Team SSEC University Of Wisconsin-Madison: VIIRS/Suomi-NPP Atmosphere L2 Cloud Properties Product. Version-1.1, NASA Level 1 and Atmosphere Archive and Distribution System Distributed Active Archive Center, https://doi.org/10.5067/VIIRS/CLDPROP_L2_VIIRS_SNPP.011, 2019.

VIIRS Atmosphere Science Team SSEC University Of Wisconsin-Madison: VIIRS/NOAA20 Atmosphere L2 Cloud Properties Product. Version-1.1, NASA Level 1 and Atmosphere Archive and Distribution System Distributed Active Archive Center, https://doi.org/10.5067/VIIRS/CLDPROP_L2_VIIRS_NOAA20.011, 2021.

Walsh, J. E., Overland, J. E., Groisman, P. Y., and Rudolf, B.: Ongoing Climate Change in the Arctic, AMBIO, 40, 6–16, https://doi.org/10.1007/s13280-011-0211-z, 2011.

Wang, D., Liang, S., Zhang, Y., Gao, X., Brown, M. G. L., and Jia, A.: A New Set of MODIS Land Products (MCD18): Downward Shortwave Radiation and Photosynthetically Active Radiation, Remote Sens., 12, 168, https://doi.org/10.3390/rs12010168, 2020.

Wendisch, M., Brückner, M., Crewell, S., Ehrlich, A., Notholt, J., Lüpkes, C., Macke, A., Burrows, J. P., Rinke, A., Quaas, J., Maturilli, M., Schemann, V., Shupe, M. D., Akansu, E. F., Barrientos-Velasco, C., Bärfuss, K., Blechschmidt, A.-M., Block, K., Bougoudis, I., Bozem, H., Böckmann, C., Bracher, A., Bresson, H., Bretschneider, L., Buschmann, M., Chechin, D. G., Chylik, J., Dahlke, S., Deneke, H., Dethloff, K., Donth, T., Dorn, W., Dupuy, R., Ebell, K., Egerer, U., Engelmann, R., Eppers, O., Gerdes, R., Gierens, R., Gorodetskaya, I. V., Gottschalk, M., Griesche, H., Gryanik, V. M., Handorf, D., Harm-Altstädter, B., Hartmann, J., Hartmann, M., Heinold, B., Herber, A., Herrmann, H., Heygster, G., Höschel, I., Hofmann, Z., Hölemann, J., Hünerbein, A., Jafariserajehlou, S., Jäkel, E., Jacobi, C., Janout, M., Jansen, F., Jourdan, O., Jurányi, Z., Kalesse-Los, H., Kanzow, T., Käthner, R., Kliesch, L. L., Klingebiel, M., Knudsen, E. M., Kovács, T., Körtke, W., Krampe, D., Kretzschmar, J., Kreyling, D., Kulla, B., Kunkel, D., Lampert, A., Lauer, M., Lelli, L., von Lerber, A., Linke, O., Löhnert, U., Lonardi, M., Losa, S. N., Losch, M., Maahn, M., Mech, M., Mei, L., Mertes, S., Metzner, E., Mewes, D., Michaelis, J., Mioche, G., Moser, M., Nakoudi, K., Neggers, R., Neuber, R., Nomokonova, T., Oelker, J., Papakonstantinou-Presvelou, I., Pätzold, F., Pefanis, V., Pohl, C., van Pinxteren, M., Radovan, A., Rhein, M., Rex, M., Richter, A., Risse, N., Ritter, C., Rostosky, P., Rozanov, V. V., Donoso, E. R., Saavedra Garfias, P., Salzmann, M., Schacht, J., Schäfer, M., Schneider, J., Schnierstein, N., Seifert, P., Seo, S.,

https://doi.org/10.5194/egusphere-2026-2210
Preprint. Discussion started: 8 May 2026

Siebert, H., Soppa, M. A., Spreen, G., Stachlewska, I. S., Stapf, J., Stratmann, F., Tegen, I., Viceto, C., Voigt, C., Vountas, M., Walbröl, A., Walter, M., Wehner, B., Wex, H., Willmes, S., Zanatta, M., and Zeppenfeld, S.: Atmospheric and Surface Processes, and Feedback Mechanisms Determining Arctic Amplification: A Review of First Results and Prospects of the (AC)^3 Project, B. Am. Meteorol. Soc., 104, E208–E242, https://doi.org/10.1175/bams-d-21-0218.1, 2023.

Wendisch, M., Crewell, S., Ehrlich, A., Herber, A., Kirbus, B., Lüpkes, C., Mech, M., Abel, S. J., Akansu, E. F., Ament, F., Aubry, C., Becker, S., Borrmann, S., Bozem, H., Brückner, M., Clemen, H.-C., Dahlke, S., Dekoutsidis, G., Delanoë, J., De La Torre Castro, E., Dorff, H., Dupuy, R., Eppers, O., Ewald, F., George, G., Gorodetskaya, I. V., Grawe, S., Groß, S., Hartmann, J., Henning, S., Hirsch, L., Jäkel, E., Joppe, P., Jourdan, O., Jurányi, Z., Karalis, M., Kellermann, M., Klingebiel, M., Lonardi, M., Lucke, J., Luebke, A. E., Maahn, M., Maherndl, N., Maturilli, M., Mayer, B., Mayer, J., Mertes, S., Michaelis, J., Michalkov, M., Mioche, G., Moser, M., Müller, H., Neggers, R., Ori, D., Paul, D., Paulus, F. M., Pilz, C., Pithan, F., Pöhlker, M., Pörtge, V., Ringel, M., Risse, N., Roberts, G. C., Rosenburg, S., Röttenbacher, J., Rückert, J., Schäfer, M., Schaefer, J., Schemann, V., Schirmacher, I., Schmidt, J., Schmidt, S., Schneider, J., Schnitt, S., Schwarz, A., Siebert, H., Sodemann, H., Sperzel, T., Spreen, G., Stevens, B., Stratmann, F., Svensson, G., Tatzelt, C., Tuch, T., Vihma, T., Voigt, C., Volkmer, L., Walbröl, A., Weber, A., Wehner, B., Wetzel, B., Wirth, M., and Zinner, T.: Overview: quasi-Lagrangian observations of Arctic air mass transformations – introduction and initial results of the HALO–(AC)^3 aircraft campaign, Atmos. Chem. Phys., 24, 8865–8892, https://doi.org/10.5194/acp-24-8865-2024, 2024.

Zhang, X., Zhao, X., Li, W., Liang, S., Wang, D., Liu, Q., Yao, Y., Jia, K., He, T., Jiang, B., Wei, Y., and Ma, H.: An Operational Approach for Generating the Global Land Surface Downward Shortwave Radiation Product From MODIS Data, IEEE Trans. Geosci. Remote Sens., 57, 4636–4650, https://doi.org/10.1109/tgrs.2019.2891945, 2019.